

# Structural basis of Irgb6 inactivation by *Toxoplasma gondii* through the phosphorylation of switch I

Hiromichi Okuma<sup>1</sup> | Yumiko Saijo-Hamano<sup>1</sup> | Hiroshi Yamada<sup>2</sup> |  
 Aalaa Alrahman Sherif<sup>3,4</sup> | Emi Hashizaki<sup>5,6</sup> | Naoki Sakai<sup>7</sup> | Takaaki Kato<sup>1</sup> |  
 Tsuyoshi Imasaki<sup>1</sup> | Satoshi Kikkawa<sup>1</sup> | Eriko Nitta<sup>1</sup> | Miwa Sasai<sup>5,6</sup> |  
 Tadashi Abe<sup>2</sup> | Fuminori Sugihara<sup>8</sup> | Yoshimasa Maniwa<sup>9</sup> |  
 Hidetaka Kosako<sup>10</sup> | Kohji Takei<sup>2</sup> | Daron M. Standley<sup>3,4</sup> |  
 Masahiro Yamamoto<sup>5,6</sup> | Ryo Nitta<sup>1</sup> 

<sup>1</sup>Division of Structural Medicine and Anatomy, Department of Physiology and Cell Biology, Kobe University Graduate School of Medicine, Kobe, Japan

<sup>2</sup>Department of Neuroscience, Graduate School of Medicine, Dentistry and Pharmaceutical Sciences, Okayama University, Okayama, Japan

<sup>3</sup>Department of Genome Informatics, Research Institute for Microbial Diseases, Osaka, Japan

<sup>4</sup>Laboratory of Systems Immunology, WPI Immunology Frontier Research Center, Osaka University, Osaka, Japan

<sup>5</sup>Laboratory of Immunoparasitology, Osaka University, Osaka, Japan

<sup>6</sup>Department of Immunoparasitology, Research Institute for Microbial Diseases, Osaka, Japan

<sup>7</sup>RIKEN SPring-8 Center, Sayo-gun, Japan

<sup>8</sup>Core Instrumentation Facility, Research Institute for Microbial Diseases, Osaka University, Osaka, Japan

<sup>9</sup>Division of Thoracic Surgery, Kobe University Graduate School of Medicine, Kobe, Japan

<sup>10</sup>Division of Cell Signaling, Fujii Memorial Institute of Medical Sciences, Tokushima University, Tokushima, Japan

## Correspondence

Masahiro Yamamoto, Laboratory of Immunoparasitology, Osaka University, Osaka, Japan.

Email: [myamamoto@biken.osaka-u.ac.jp](mailto:myamamoto@biken.osaka-u.ac.jp)

Ryo Nitta, Division of Structural Medicine and Anatomy, Department of Physiology and Cell Biology, Kobe University Graduate School of Medicine, Kobe, Japan.

Email: [ryonitta@med.kobe-u.ac.jp](mailto:ryonitta@med.kobe-u.ac.jp)

## Funding information

Japan Agency for Medical Research and Development, Grant/Award Numbers: JP20am0101108, JP23fk0108682, JP223fa627002, JP22wm0325010,

## Abstract

Irgb6 is a priming immune-related GTPase (IRG) that counteracts *Toxoplasma gondii*. It is known to be recruited to the low virulent type II *T. gondii* parasitophorous vacuole (PV), initiating cell-autonomous immunity. However, the molecular mechanism by which immunity-related GTPases become inactivated after the parasite infection remains obscure. Here, we found that Thr95 of Irgb6 is prominently phosphorylated in response to low virulent type II *T. gondii* infection. We observed that a phosphomimetic T95D mutation in Irgb6 impaired its localization to the PV and exhibited reduced GTPase activity in vitro. Structural analysis unveiled an atypical conformation of nucleotide-free Irgb6-T95D, resulting from a conformational change in the G-domain that allosterically modified the PV membrane-binding interface. In silico docking corroborated the disruption of the physiological membrane binding site. These

Hiromichi Okuma and Yumiko Saijo-Hamano contributed equally to this work.

This is an open access article under the terms of the [Creative Commons Attribution-NonCommercial-NoDerivs](https://creativecommons.org/licenses/by-nc-nd/4.0/) License, which permits use and distribution in any medium, provided the original work is properly cited, the use is non-commercial and no modifications or adaptations are made.

© 2023 The Authors. *Genes to Cells* published by Molecular Biology Society of Japan and John Wiley & Sons Australia, Ltd.

JP21gm0810013, JP21am0101070; Japan Society for the Promotion of Science, Grant/Award Numbers: 19H00970, 19H04809, 20B304, 21H05254, 21K06988, 21K19352, 22H02795; Moonshot Research and Development Program, Grant/Award Number: JPMJMS2024

**Communicated by:** Shigeo Koyasu

findings provide novel insights into a *T. gondii*-induced allosteric inactivation mechanism of Irgb6.

#### KEYWORDS

allosteric conformational change, immune-related GTPase, Irgb6, phosphorylation, *Toxoplasma gondii*, x-ray crystallography

## 1 | INTRODUCTION

Interferon- $\gamma$  (IFN- $\gamma$ )-inducible immunity-related GTPases (IRGs) are phylogenetically related to the dynamin GTPase superfamily (Kim et al., 2012; Praefcke & McMahon, 2004). These GTPases are activated by self-assembly /polymerization or by the presence of a lipid membrane (Hunn et al., 2008; Praefcke & McMahon, 2004; Prakash et al., 2000; Yamada et al., 2022). Self-assembly of IRGs occurs via the G-domain as an interface, and each molecule acts as a GTPase-activating protein (Pawlowski et al., 2011; Yamada et al., 2022). This process is nucleotide-sensitive through the conformational change of switches I and II, which affects the self-assembly interface in the G-domain and relays this information to the membrane binding interface in the N- and C-domains (Saijo-Hamano et al., 2021). Our previous biochemical and electron microscopic analyses also proved the nucleotide dependence of membrane targeting and deformation; An IRG called Irgb6 without nucleotide can target the membrane, whereas GTP-binding to Irgb6 severely deforms the membrane (Yamada et al., 2022).

*Toxoplasma gondii* is an important pathogen for warm-blooded animals, including humans. It enters host cells and forms a membrane-bounded structure called the parasitophorous vacuole (PV; Boothroyd, 2009; Goldstein et al., 2008). In response to low virulent type II *T. gondii* infection, the host immune system expresses IFN- $\gamma$ , which stimulates cell-autonomously immunity to kill the microorganism and thus inhibit the intracellular growth of *T. gondii* (Divanovic et al., 2012; Sasai et al., 2018; Scharton-Kersten et al., 1997). In mouse cells, two subfamilies of IFN-inducible GTPases such as IRGs and guanylate-binding proteins (GBPs) are well known to specifically target the PV membrane (PVM) and disrupt the PV in which *T. gondii* is enfolded (Howard et al., 2011; Khaminets et al., 2010; MacMicking, 2012; Saeij & Frickel, 2017; Yamamoto et al., 2012). Among IFN-inducible GTPases, Irgb6 directly recognizes the phospholipid PI5P, which accumulates on *T. gondii* PVMs and plays a pioneering role in recruiting other IFN-inducible GTPases such as Irga6, Irgb10, and GBPs as well as effectors such as p62/Sqstm1 and ubiquitin to the PVM (Lee et al., 2020; Saijo-Hamano et al., 2021). Thus, Irgb6 elicits

the downstream IFN-inducible GTPases- and effectors-dependent cell-autonomous responses. In order to counter the host cell-autonomous defense system, virulent type I *T. gondii* secretes various effector proteins including serine-threonine kinases, ROP17 and ROP18, which phosphorylate host Irga6 and Irgb6 at two conserved threonine residues in the switch I region, biochemically abrogating the GTPase activity of IRGs and inhibiting the recruitment of IRGs to the PVM, thus rendering IRGs inactive (Etheridge et al., 2014; Fentress et al., 2010; Steinfeldt et al., 2010). Therefore, the inactivation of IRGs by ROP17 and ROP18 together with a polymorphic pseudo-kinase ROP5 is well established by biochemical and cell biological evidence in virulent type I *T. gondii* infection (Behnke et al., 2011; Behnke et al., 2012; Reese et al., 2011). However, the mechanism of how the cell-autonomous immune system is inactivated in response to low virulent type II *T. gondii* infection remains unclear.

To explore the mechanisms of IRG inactivation in response to type II *T. gondii* infection, we randomly searched for posttranslational protein modifications about Irgb6 that occur after the infection and found that Thr95 of Irgb6 is prominently phosphorylated. Then we investigated the effect of Thr95 phosphorylation using Irgb6 with a phosphomimetic mutation of Thr95 to aspartate, which was shown to have an identical impact on Irga6 as phosphor-threonine (Steinfeldt et al., 2010). Consequently, the mutant was rarely recruited to the PVM in cells and had impaired GTPase activity. Biochemical and electron microscopic studies further demonstrated the inability of the mutant to form polymers and no GTPase activation by the lipid membranes. Now that we have shown that Irgb6 is inactivated by Thr95 phosphorylation, the next step is to clarify the structural basis for the inactivation of Irgb6. The crystal structure of Irgb6 with T95D mutation further showed that the G-domain of the mutant exhibited an atypical nucleotide-free conformation, presumably associated with the interruption of the GTPase cycle. Surprisingly, the conformational change of the G-domain allosterically modified the conformation of the membrane-binding interface on the opposite side of the protein, thus providing a mechanism by which phosphorylation of Thr95 inhibits physiological PI5P binding.

## 2 | RESULTS

### 2.1 | Type II *T. gondii* induces phosphorylation of Thr95 on Irgb6 that inhibits its recruitment to PVM

To identify the posttranslational modification sites on Irgb6 induced by type II low virulent *T. gondii*, Spot-tagged Irgb6 in mouse embryonic fibroblast (MEF) cells infected with type II *T. gondii* was immunoprecipitated with anti-Spot nanobody-coupled beads, digested with trypsin, and analyzed by LC-MS/MS. This analysis revealed a phosphopeptide containing phosphorylated Thr95 (Figure 1a). The Thr95-phosphorylated peptide was detected in immunoprecipitates from *T. gondii*-infected cells but not from uninfected cells (Figure 1b), confirming that the phosphorylation of Thr95 on Irgb6 was induced by *T. gondii* infection.

To assess the effect of phosphorylation of the Thr95 on Irgb6, the Flag-tagged wild-type or a phosphomimetic T95D mutant of Irgb6 (Irgb6-T95D) was expressed in Irgb6-deficient MEFs (Figure 2a). An indirect immunofluorescence study showed that Flag-tagged wild-type Irgb6 (Irgb6-WT) was loaded onto PVM of the low virulent type II ME49 *T. gondii* strain (Figure 2b), which is consistent with the strain-specific loss of ability for to phosphorylate IRG by ROP18 (Fentress et al., 2010; Steinfeldt et al., 2010). In sharp contrast, Flag-tagged Irgb6-T95D was not detected on the *T. gondii* PVM (Figure 2b), suggesting that the phosphorylation of Thr95 of Irgb6 prevents localization on the PVM. Next, we examined the effect of Thr95 phosphorylation on the recruitment of another IFN-inducible GTPase Irga6 (Figure 2c). The recruitment of Irga6 was not observed upon reconstitution of Irgb6-T95D in Irgb6-deficient MEFs (Figure 2c). IFN- $\gamma$  stimulates the coating of effectors such as ubiquitin and p62/Sqstm1 on *T. gondii* PVM in a manner dependent on IFN-inducible GTPases (Haldar et al., 2015; Lee et al., 2015). Therefore, we next analyzed whether the loading of ubiquitin and p62/Sqstm1 was affected by Thr95 phosphorylation (Figure 2c). Although reconstitution of Irgb6-WT recovered effector loading on *T. gondii* PVMs in Irgb6-deficient MEFs, reconstitution of Irgb6-T95D did not (Figure 2c). Taken together, these data indicate that Thr95 phosphorylation of Irgb6 prevents recruitment to the low virulent type II *T. gondii* PVM.

### 2.2 | Irgb6-T95D mutation disrupts GTPase activity and GTP-induced polymer formation

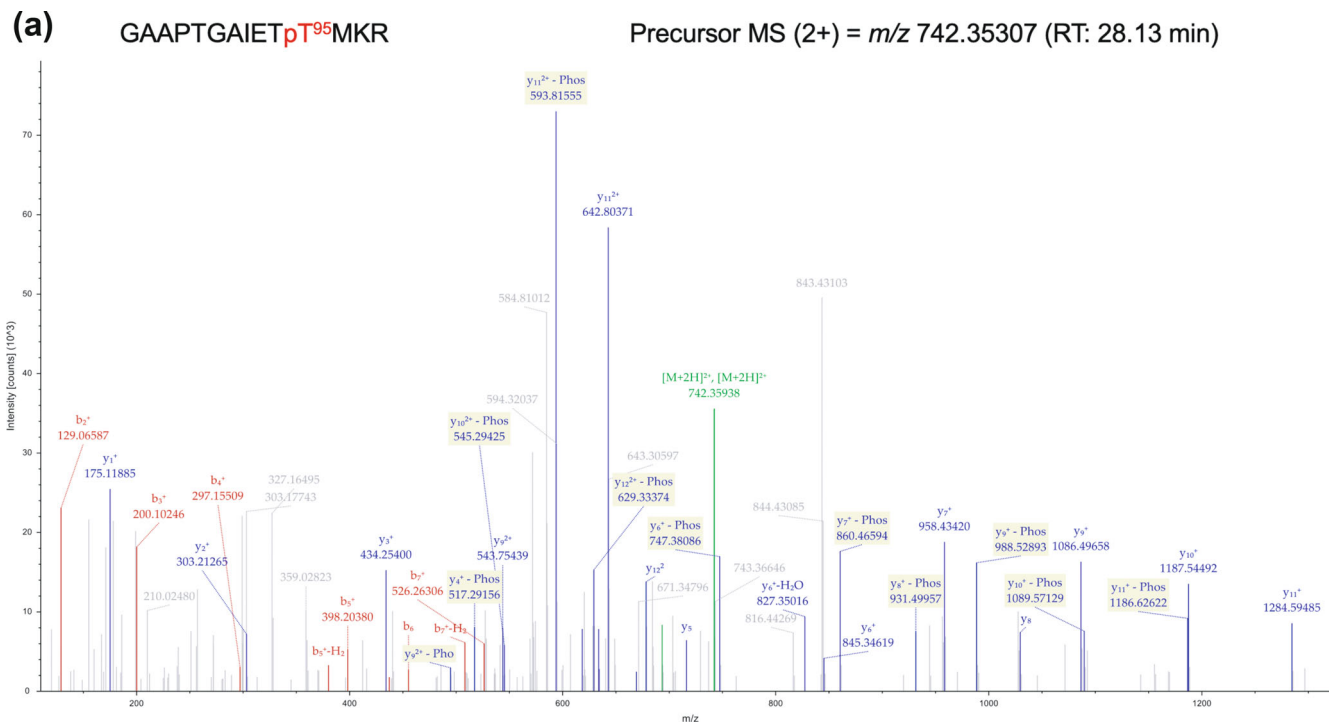
We then investigated the effect of phosphorylation of the Thr95 on Irgb6 GTPase. We purified Irgb6-WT and

Irgb6-T95D through anion exchange chromatography. Size exclusion chromatography (SEC) of purified Irgb6-T95D produced two peaks, similar to Irgb6-WT (Figure S1A; Saijo-Hamano et al., 2021). SDS-PAGE analysis indicated that Irgb6-T95D was mainly eluted in the second peak. Since the estimated molecular weight of Irgb6-T95D is 47.3 kDa, the eluted Irgb6-T95D in the second peak was assumed to be the monomer used for further in vitro functional and structural assays.

The GTPase activity was roughly checked by the endpoint assay of GTP hydrolysis to GDP after coincubation of 100  $\mu$ M Irgb6 and 100  $\mu$ M GTP in the 150 mM NaCl-containing buffer for 30 min at 37°C. Irgb6-WT hydrolyzed two thirds of GTP to GDP, whereas Irgb6-T95D hydrolyzed only about 10% of GTP to GDP (Figures 3b and S1B). This indicates that the phosphomimetic mutation of Thr95 (T95D) in the switch I region of Irgb6 significantly reduced the GTPase activity of Irgb6, although the basal GTPase activity of even Irgb6-WT was also extremely slow.

We then followed the time course of GTP hydrolysis by Irgb6-WT and Irgb6-T95D. The effects of ionic strength or the presence of lipid membranes on the GTPase activity were also examined (Yamada et al., 2022). Inorganic phosphate released by 20  $\mu$ M Irgb6 was measured in 0 or 100 mM NaCl or in the presence of PI5P-containing liposomes (Figure 3a,b). The estimated basal GTPase rate of Irgb6-WT was 0.08–0.1/min, and that of Irgb6-T95D was  $\sim$ 5-fold lower than Irgb6-WT ( $\sim$ 0.02/min). Those are much slower than the reported rates of dynamin GTPase (12/min; Shpetner & Vallee, 1992) and G-protein (2–4/min; Bourne et al., 1990). The ionic strength did not have much effect on the GTPase rates of Irgb6-WT nor Irgb6-T95D, at least in the tested experimental conditions (Figure 3a). On the other hand, the addition of liposomes increased the GTPase activity of Irgb6-WT more than 2-fold. In contrast, no effect on Irgb6-T95D was observed by the addition of liposomes, consistent with the distinct localization of Irgb6-WT and Irgb6-T95D within the cell (Figure 2a).

We further examined the binding of 2'/3'-O-(*N*-Methyl-anthraniloyl)-guanosine-5'-diphosphate (mant-GDP) and 2'/3'-O-(*N*-Methyl-anthraniloyl)-guanosine-5'-( $\gamma$ -thio)-triphosphate (mant-GTP $\gamma$ S) by equilibrium titration. Both Irgb6-WT and Irgb6-T95D bound mant-GDP and mant-GTP $\gamma$ S similarly in the micromolar range, indicating that the T95D mutation did not affect the nucleotide-binding ability of the protein (Figures 3c and S2). The binding pattern of Irgb6, in which there is little difference in affinity for GDP and GTP, sharply contrasts that of Irga6, which was reported to exhibit a 10-fold preference for GDP over GTP (Uthaiyah et al., 2003).



(b) EIC (extracted ion chromatogram) of  $m/z$  742.35307  $\pm$  5 ppm

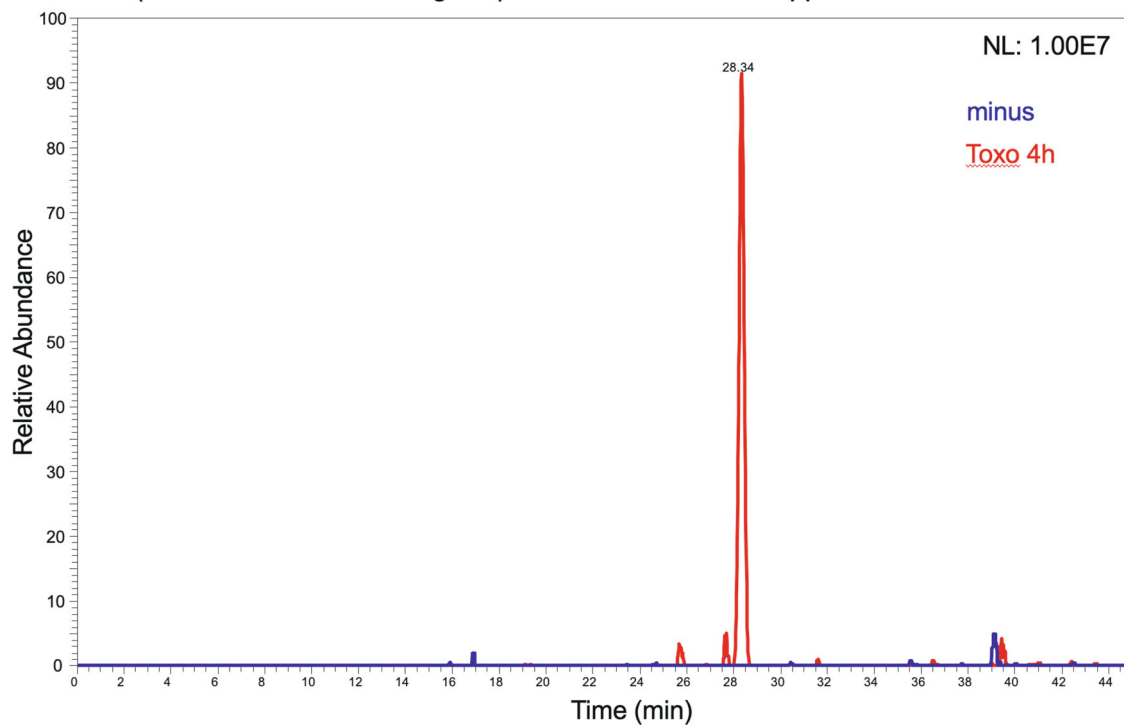


**FIGURE 1** Phosphorylation of Irgb6 at Thr95 is induced by *T. gondii* infection. (a) Irgb6-deficient mouse embryonic fibroblasts stably expressing Spot-tagged Irgb6 were infected with *T. gondii* and subjected to immunoprecipitation with anti-Spot nanobody followed by tryptic digestion and LC-MS/MS analysis. Phosphorylation of Thr95 was demonstrated by the MS/MS spectrum of the  $m/z$  742.35307 precursor ion at a retention time of 28.13 min. Fragmented b-ions and y-ions are shown in red and blue, respectively. The unfragmented ion is shown in green. Fragment ions with neutral loss of phosphate and water are shown as "...Phos" and "-H<sub>2</sub>O", respectively. (b) The extracted ion chromatogram of  $m/z$  742.35307 corresponds to the doubly charged Irgb6 phosphopeptide (GAAPTGAIE<sub>p</sub>T<sup>95</sup>MKR), which was induced by *T. gondii* infection.

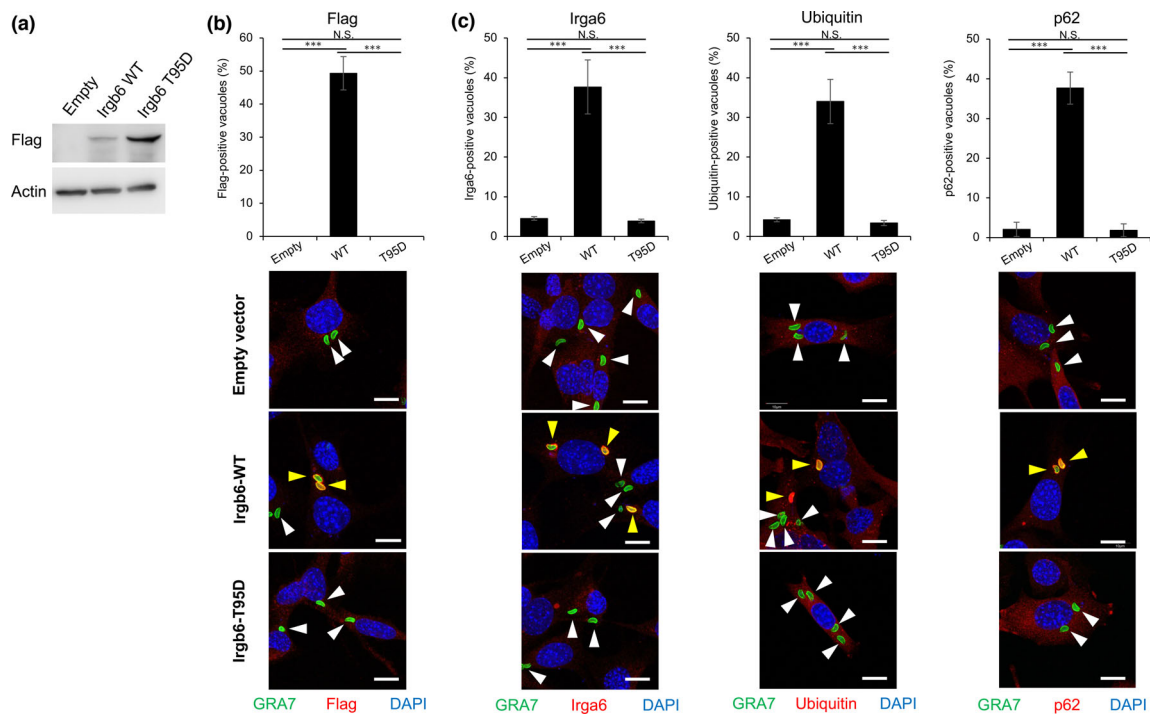


**FIGURE 2** Irgb6 T95D mutation abrogates recruitment of Irgb6, other Interferon-inducible GTPases and effectors. (a) The expression of Irgb6-WT and Irgb6-T95D. (b and c) Confocal microscope images of Flag (b) or indicated proteins (c) accumulation on parasitophorous vacuoles (PVs) in mouse embryonic fibroblast (MEFs) after parasite infection. Percentage of Flag- or indicated proteins-positive PVs in cells infected with ME49 parasites. A total of 100 PVs were counted in each sample. All images are representative of three independent experiments. Yellow and white arrowheads indicate *T. gondii* PV membrane (green) with and without indicated antibodies (red), respectively. Scale bars, 10  $\mu$ m.

The oligomerization of Irgb6-WT and Irgb6-T95D in the nucleotide state was verified using mass photometry (MP; Figure 3d,e). Protein samples were incubated at 37°C for 20 min and then measured. In the nucleotide-free state, both Irgb6-WT and Irgb6-T95D were monomeric. Adding GDP plus  $\text{AlF}_3$  (mimicking GDP-Pi-bound form) to Irgb6-WT induced dimerization of ~10% Irgb6-WT, whereas Irgb6-T95D remained a monomer. Polymer formation upon GTP binding was further observed by negative stain electron microscopy. In the Irgb6-WT, no polymer formation was observed before the addition of nucleotide (Figure 3f). The addition of GTP analog Guanosine-5'-[( $\beta,\gamma$ -imido]triphosphate (GMP-PNP) or GDP plus  $\text{AlF}_3$  induced irregular polymer formation represented by the high-density areas. On the other hand, Irgb6-T95D showed minimal polymer formation even after the addition of GMP-PNP or GDP plus  $\text{AlF}_3$  (Figure 3g). Considering that the GTP-binding ability was not affected by the T95D mutation (Figure 3c), this result suggested that a conformational change after the binding of GTP is required for polymer formation and that this change was inhibited by the phosphomimetic mutation of Thr95.

### 2.3 | Crystal structures of Irgb6-T95D in the GTP-bound and nucleotide-free states

The experiments above showed that phosphorylation of Thr95 in the switch I region, which was mimicked by the T95D mutation, inhibited the recruitment of Irgb6 and related molecules, including ubiquitin, to the *T. gondii* PVM (Figure 2). The T95D mutation also significantly reduced the GTPase activity of Irgb6 (Figure 3). Although Irgb6-T95D exhibited binding to GTP and GDP similar to Irgb6-WT, neither polymer formation nor GTPase activation by the membrane was observed in the mutant (Figure 3). This suggests that a conformational change after GTP binding, namely isomerization, is less likely to occur in Irgb6-T95D; as a result, membrane binding is decoupled from GTPase cycling. However, since the membrane-binding interface is located in the C-domain, more than 50 Å from residue 95, this raises the difficult question of how T95 phosphorylation affects the conformation of the membrane-binding interface. To address this question, we tried to crystallize Irgb6-T95D with various nucleotides, including GTP, GDP, GMPPNP, GTP- $\gamma$ S, and without nucleotide. Among them, we successfully

crystallized the Irgb6-T95D in the GTP-bound and nucleotide-free states, the same nucleotide states as the reported structures of Irgb6-WT (Saijo-Hamano et al., 2021).

The crystal structures of Irgb6-T95D were solved with GTP (Irgb6-T95D-GTP) and without nucleotide (nucleotide-free [NF]) (Irgb6-T95D-NF) at 1.68 and 2.05 Å resolution, respectively (Figure 4a,b and Table 1). The former

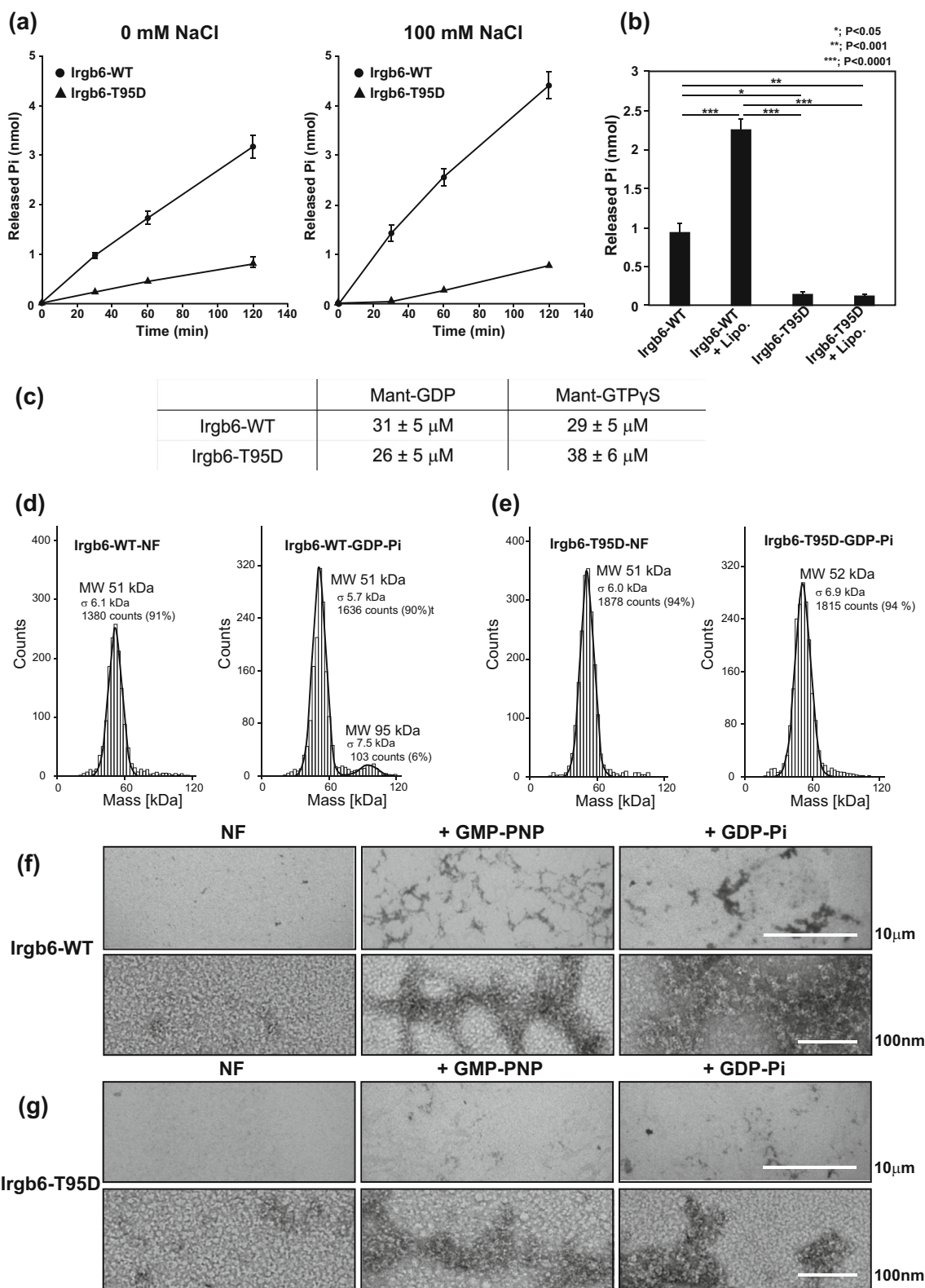


FIGURE 3 Legend on next page.

structure possessed GTP or, in part, a hydrolyzed product GDP in the nucleotide-binding pocket without stable  $Mg^{2+}$  and surrounded water density (Figures 5a and S3). The latter had neither nucleotide nor ion in the pocket (Figure 5b,c).

Irgb6-T95D-GTP was superposed with Irgb6-WT-GTP using all main chain atoms (Figure 4c). Irgb6-T95D-GTP adopted the same conformation as Irgb6-WT-GTP, with an overall root mean square deviation (RMSD) from Irgb6-WT-GTP of 0.27 Å (Figure 4f). GTP in the Irgb6-WT and -T95D is trapped at the atypical position, shifting toward the G5 nucleotide-binding motif, probably because of the Irgb6-specific Val220 in the G5 motif (Figure S3). This shift keeps GTP distant from the switch I and II regions, failing to trap the  $Mg^{2+}$  ion and slowing its basal GTPase rate tremendously (Figure 3a). As described in the previous report (Saijo-Hamano et al., 2021), we call this atypical Irgb6-T95D-GTP complex a “collision complex.” Dimerization may change the conformations of G4 and G5 motifs to fit GTP ready to be hydrolyzed, the “isomerization reaction.”

Irgb6-T95D-NF-molA and -molB were superposed with Irgb6-WT-NF using all main chain atoms (Figure 4d). In contrast to the GTP-bound form, the Irgb6-T95D-NF form exhibited a considerably different conformation from the WT (Figure 4b,d,e). The crystal of Irgb6-T95D-NF included two molecules in the asymmetric unit, referred to here as molA and molB. Both molA and molB exhibited high RMSDs from Irgb6-WT-NF. A domain-by-domain comparison showed that the G-domain of Irgb6-T95D-NF appeared to be more similar to Irgb6-WT-GTP than Irgb6-WT-NF. The N-domain of Irgb6-T95D-NF was relatively similar to Irgb6-WT-NF; however, the C-domain took on a considerably different conformation (Figure 4d,f). Specifically, the following changes occurred in the C-domain: stabilization of the PVM-binding loop, elongation of helix  $\alpha$ -La by one turn, and a unique conformation of the  $\alpha$ K- $\alpha$ La loop, such that

it was inserted into the space between the three helices  $\alpha$ A,  $\alpha$ F, and  $\alpha$ La (Figure 4d, inset).

The stabilization of the PVM-binding loop might be affected by the crystal packing environment (Figure S4) since PVM-binding loops from molA and molB interact with each other to form a dimer. On the other hand, the elongation of  $\alpha$ -La as well as the unique  $\alpha$ K- $\alpha$ La loop, are more likely to be influenced by the environment surrounding the three helices  $\alpha$ A,  $\alpha$ K, and  $\alpha$ La. Thus, we next examined the conformational changes of nucleotide-free WT and mutant Irgb6 in solution using hydrogen-deuterium exchange mass spectrometry (HDX-MS; Figures 6 and S5). Comparison of HDX rates in WT and T95D Irgb6 can reveal conformational changes in solution at the residue level. We evaluated the impact of the T95D mutation on the differences in exchange rates of Irgb6 in the nucleotide-free state.

Consequently, the greatest differences in deuterium uptake between Irgb6-WT-NF and Irgb6-T95D-NF were found to be concentrated around T95D in the G-domain and the membrane-binding surface in the C-domain (Figure 6a,b). In particular, a significant difference was observed for Tyr370, which is exposed on the surface in a flexible loop in Irgb6-WT-NF but internalized in helix  $\alpha$ -La in Irgb6-T95D-NF crystal structure. Indeed, the HDX-MS results agreed perfectly with the crystal structures, strongly implying that the conformational changes observed in the T95D-NF crystal structure were not artifacts of crystal packing but occurred in solution as well. In the next section, we focus on the structural details of Irgb6-T95D-NF form.

## 2.4 | Irgb6-T95D adapts an atypical Apo-form

As described above, the structure of the G-domain of Irgb6-T95D-NF differed significantly from that of

**FIGURE 3** Biochemical property of Irgb6-T-95D. (a) GTPase activity of Irgb6-WT or Irgb6-T95D under the distinct ionic-strength conditions (0 and 100 mM NaCl). Released inorganic phosphate by Irgb6 GTPase was determined at 30, 60, and 120 min. The values are expressed in mean  $\pm$  SEM from three independent experiments. (b) Loss of PI5P-dependent stimulatory effect of GTPase activity by Irgb6-T95D. Irgb6-WT or Irgb6-T95D was incubated in the presence or absence of PI5P-containing liposomes under high ionic strength conditions at 37°C for 15 min. The values are expressed in mean  $\pm$  SEM from three independent experiments. (c) Nucleotide-binding properties of Irgb6-WT and Irgb6-T95D.  $K_d$  value ( $\mu$ M) was measured by equilibrium titration. The mean values of two independent experiments are shown. See Figure S2 for details. (d) Mass distribution for 25 nM Irgb6-WT in the nucleotide-free state (left) and in the GDP-Pi state with GDP-AlF<sub>3</sub> (right). Data are representative of two independent experiments. (e) Mass distribution for 25 nM Irgb6-T95D in the nucleotide-free state (left) and in the GDP-Pi state with GDP-AlF<sub>3</sub> (right). Data are representative of two independent experiments. (f) Electron micrographs showing guanine nucleotide-dependent polymer formation of Irgb6-WT. Images are shown at low magnification (upper panels), and at high magnification (bottom panels). Data are representative of three independent experiments. Note that polymerization of Irgb6-WT is visible in the presence of non-hydrolyzable GTP analog (GMP-PNP) or GDP-phosphate condition (GDP-Pi), but not in nucleotide-free condition (NF). (g) Decreased nucleotide-dependent polymer formation of Irgb6-T95D. Images are shown at low magnification (upper panels), and at high magnification (bottom panels). Data are representative of three independent experiments.

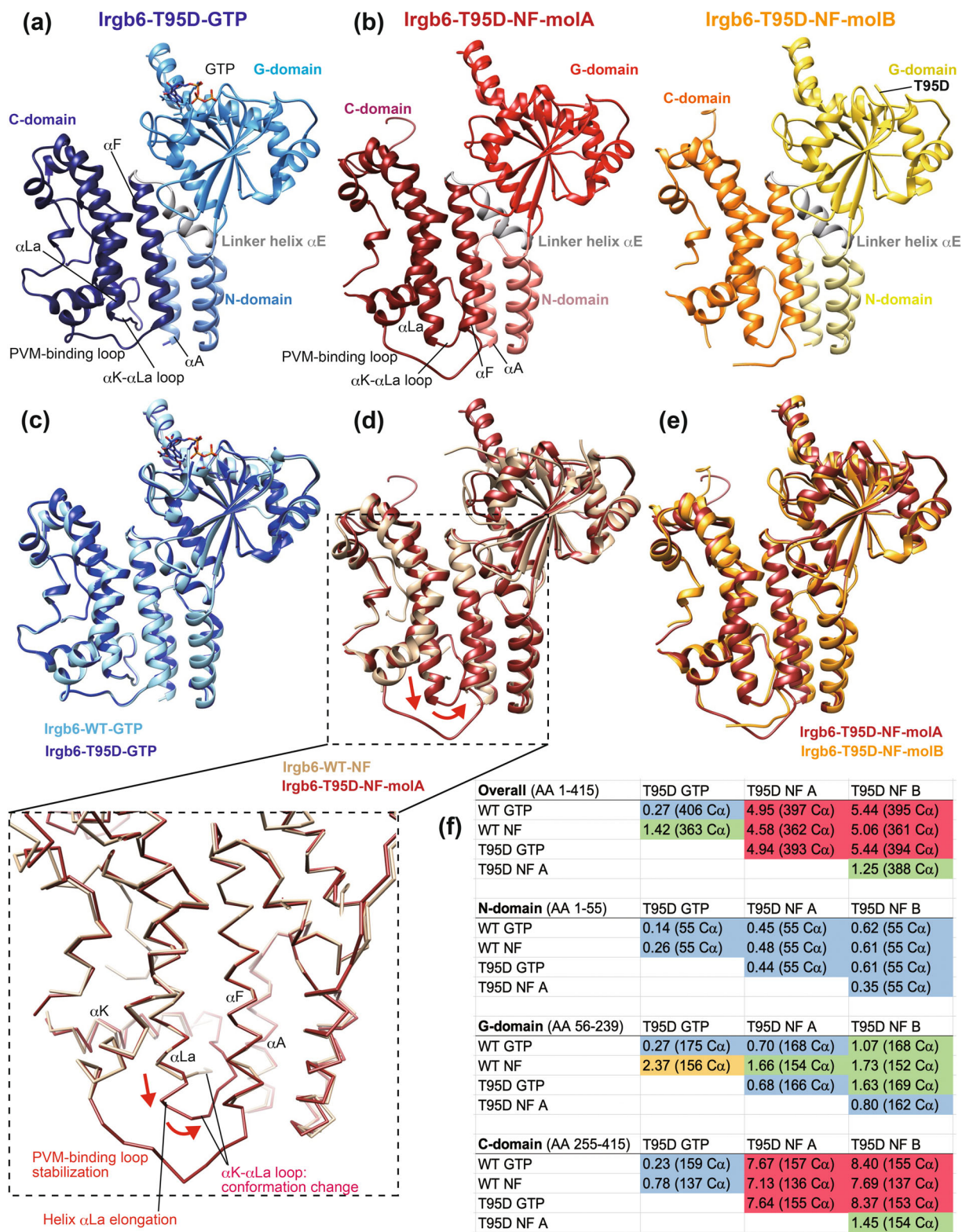


**FIGURE 4** Crystal Structures of Irgb6-T95D with GTP and without any nucleotide. (a) Crystal structure of Irgb6-T95D-GTP. (b) Crystal structure of Irgb6-T95D-NF. Left, Irgb6-T95D-NF-molA; right, Irgb6-T95D-NF-molB. (c) Comparison of Irgb6-T95D-GTP (blue) with Irgb6-WT-GTP (light blue; PDB ID 7VEX). (d) Comparison of Irgb6-T95D-NF-molA (red) with Irgb6-WT-NF (light brown; PDB ID 7VES). (e) Comparison of Irgb6-T95D-NF-molA (red) with Irgb6-T95D-NF-molB (yellow). (f) root mean square deviations (RMSDs) among Irgb6-WT and Irgb6-T95D. Overall RMSDs and RMSD values superimposed on their N-, G-, and C-domains are shown. Number of atoms used in the RMSD calculation is shown in parentheses. RMSDs  $\leq$  1: blue,  $1 <$  RMSDs  $\leq$  2: green,  $2 <$  RMSDs  $\leq$  3: yellow,  $3 <$  RMSDs  $\leq$  4: orange,  $4 <$  RMSDs: red. PVM, parasitophorous vacuole membrane.

TABLE 1 Data collection and refinement statistics.

	Irgb6-T95D-GTP	Irgb6-T95D-NF
Data collection		
Space group	P2 <sub>1</sub> 2 <sub>1</sub> 2 <sub>1</sub>	P2 <sub>1</sub> 2 <sub>1</sub> 2 <sub>1</sub>
Unit cell parameter		
a, b, c (Å)	69.122, 75.750, 80.277	71.532, 80.613, 147.649
α, β, γ (°)	90, 90, 90	90, 90, 90
Resolution range (Å)	50.000–1.67 (1.78–1.68)	50.00–2.04 (2.17–2.05)
Completeness (%)	99.8 (99.1)	99.4 (97.6)
R-merge (%)	12.2 (191.6)	11.8 (177.1)
R-meas (%)	13.2 (207.2)	12.8 (190.8)
<I/σ(I)>	11.55 (0.98)	10.25 (0.96)
CC <sub>1/2</sub>	99.8 (47.5)	99.8 (50.8)
Multiplicity	6.90 (6.93)	6.95 (7.15)
Refinement		
Resolution range (Å)	37.88–1.68 (1.72–1.68)	40.55–2.05 (2.10–2.05)
No. Reflections	49,012 (3396)	54,351 (3645)
R-work/R-free	0.2059 (0.3844)/0.2302 (0.4215)	0.2256 (0.3167) /0.2828 (0.3710)
No. atoms		
Protein	3286	6392
Water	167	97
Ligands	32	—
RMS (bonds) (Å)	0.008	0.008
RMS (angles) (°)	0.921	0.886
Ramachandran plot (%)		
Favored	97.24	97.03
Allowed	2.76	2.97
Outliers	0.00	0.00
Rotamer outliers (%)	0.28	1.00
Average B-factor (Å <sup>2</sup> )	38.45	56.88
Protein	38.32	57.02
Water	38.48	47.28
Ligands	52.39	—

Irgb6-WT-NF. These differences were readily visible in the active site of the G-domain in the electron density map (Figure 5). It should be noted that the resolution of both structures was ~2.0 Å.

In Irgb6-WT-NF, the P-loop underwent a loop-to-helix transition, which further induced conformational changes around the active site, including the helix-to-loop transition of helix α<sub>d</sub>, as reported previously (Figure 5d; Saijo-Hamano et al., 2021). Notably, a dense hydrogen-bonding network via several water molecules connected switch I residue Thr95 and Thr99 to helix H1 to stabilize the active site conformation in the WT-NF form (Figure 5d). On the other hand, in Irgb6-T95D-NF, T95D is flexible and cannot be visualized in molA (Figure 5b) while it faces outward in molB (Figure 5c), indicating that a stable hydrogen bonding network is not formed in Irgb6-T95D-NF. Consequently, the P-loop is in a similar arrangement to the collision GTP state (molA) or becomes flexible (molB); thus, Irgb6-T95D-NF cannot take on the physiologically-required nucleotide-free form. This arrangement of the P-loop rotates the helix H1 in a clockwise direction, inducing a conformational change in the H1–S2 and S6–H5 loops (Figure 5e). These loops serve as an interface for the linker helix α<sub>E</sub>, further transducing the N- and C-domain changes described below.

## 2.5 | Thr95 phosphorylation alters the conformation of the PVM-binding region

Next, to examine how structural changes in the active site of the G-domain propagate to the N- and C-domains, Irgb6-T95D-NF and Irgb6-WT-NF were aligned with the G-domain as a reference. Consequently, we observed a clockwise rotation of N- and C-domains around the G-domain (Figure 7a and Movie S1). The conformational change of the helix H1 and H1–S2 loop caused by a loss of a hydrogen-bonding network around T95 was transmitted to the linker helix α<sub>E</sub>. The rightward movement of α<sub>E</sub> (black-dotted arrow in Figure 7a) further induced a rotation of the N- and C-domains (blue and magenta-dotted arrow in Figure 7a). In this process, hydrophilic, ionic, and hydrophobic bonds among the linker helix α<sub>E</sub>, G-domain (H1 and H1–S2), N-domain (α<sub>A</sub> and α<sub>C</sub>), and C-domain (α<sub>F</sub> and La) were rearranged (Figures 7b and S6). The resulting rotation angles of the N-terminal helices α<sub>A</sub>–α<sub>C</sub> were relatively more extensive than those of the helices in the C-domain so that the groove between α<sub>A</sub> (N-domain) and α<sub>F</sub> (C-domain) was widened along with the flipping of Trp3 (Figures 7c,d and S7). The widening of the groove between the N- and C-domains was consistent with the HDX-MS results, which showed an increased deuterium exchange rate in the N-terminal half of α<sub>C</sub> (Figure 6b, amino acids 34–43). Due to these changes, the α<sub>K</sub>–α<sub>La</sub> loop could be inserted into the widened groove, further stabilizing the elongated form of helix α<sub>La</sub> through hydrophobic contact between Trp3 and Val364.

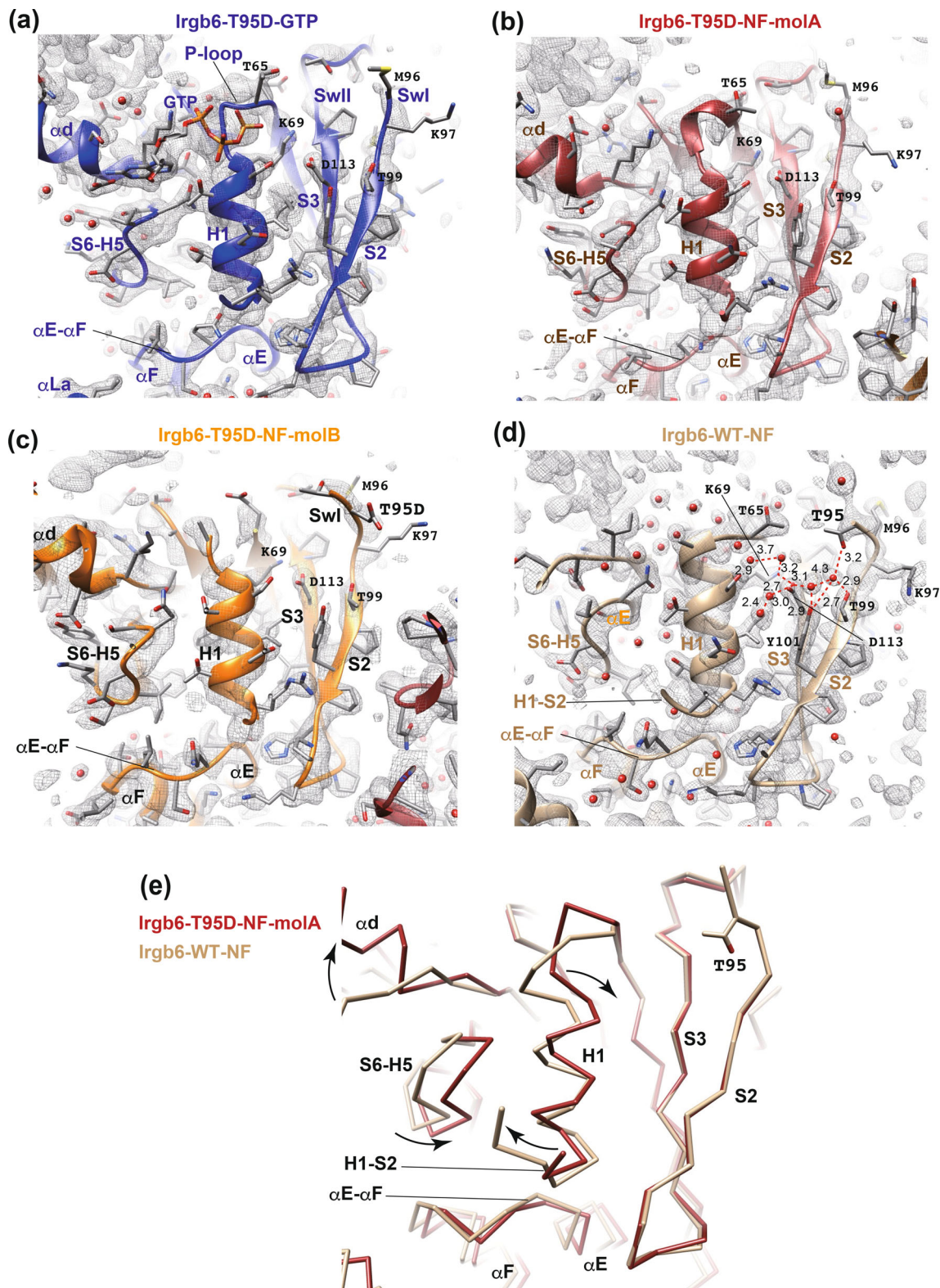


**FIGURE 5** Nucleotide-binding pocket of Irgb6-T95D. The 2fo-fc maps around the nucleotide-binding pocket were shown at the contour level of 1.2  $\sigma$ . (a) Irgb6-T95D-GTP. Phosphates in GTP are buried in the P-loop. (b) Irgb6-T95D-NF-molA. P-loop takes a similar structure as Irgb6-T95D-GTP. T95D is invisible because of its flexibility. (c) Irgb6-T95D-NF-molB. P-loop is invisible because of its flexibility. T95D faces outward and water-mediated hydrogen bonding was not observed. (d) Irgb6-WT-NF. Compared with Irgb6-T95D-GTP (a), the loop-to-helix transition of the P-loop was observed. Thr95 faces toward the P-loop and contributes to dense water-mediated hydrogen bonding. (e) Conformational change of Irgb6-NF around the nucleotide-binding pocket by T95D mutation. Note that the secondary structures of the G-domain of IRGs are named in S1–S6 ( $\beta$ -sheet) and H1–H5 ( $\alpha$ -helix), whereas those of N- and C-domains are named in  $\alpha$ A– $\alpha$ Lb ( $\alpha$ -helix).

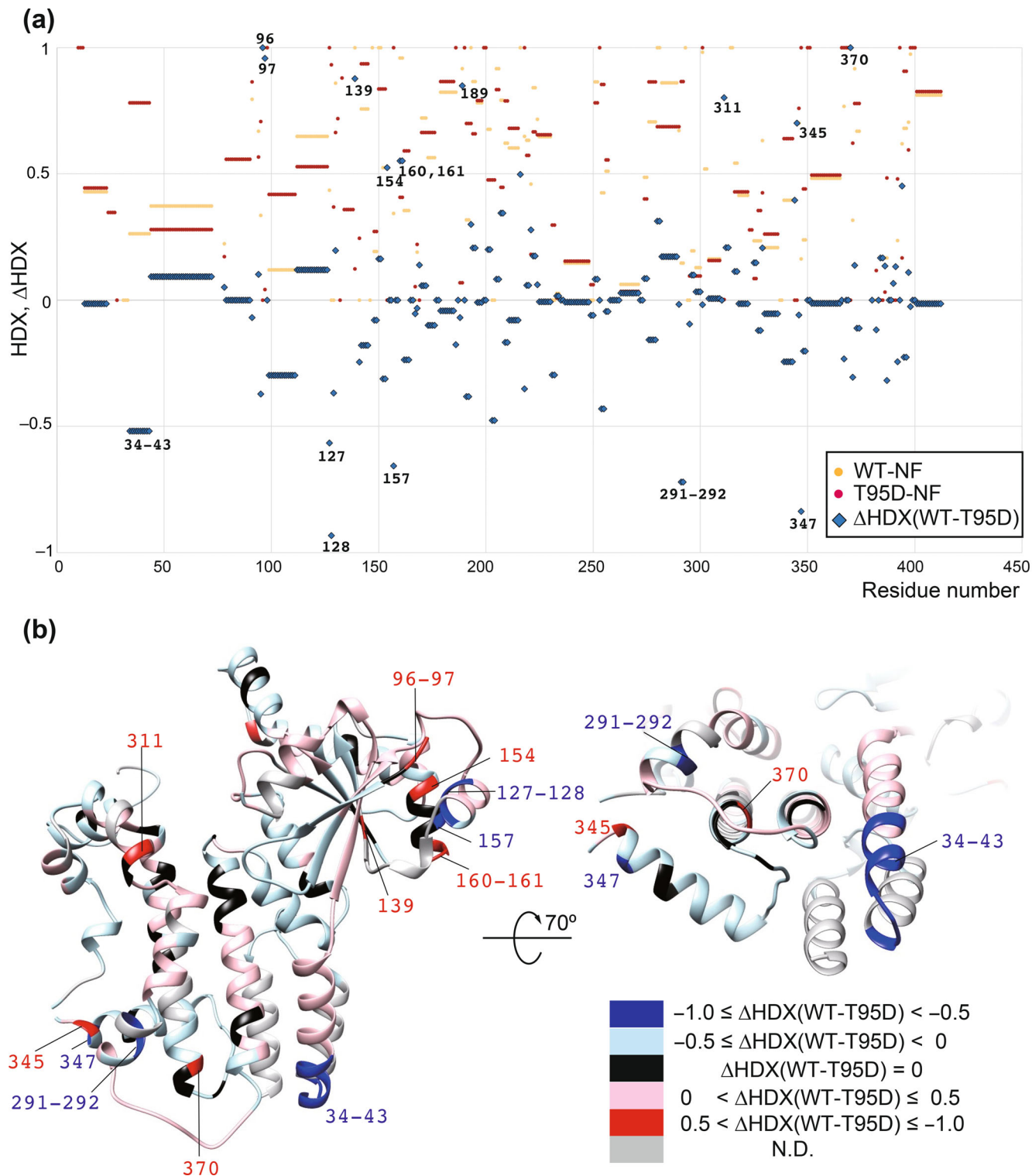


**FIGURE 6** Conformational change induced by T95D mutation depicted by the comparison of hydrogen-deuterium exchange (HDX) rates between Irgb6-WT-NF and Irgb6-T95D-NF. (a) HDX-rates of Irgb6-WT-NF (light brown) and Irgb6-T95D-NF (red), shown with the  $\Delta$ HDX (blue) which represents the difference in the HDX rates between WT and T95D. (b) Irgb6-T95D-NF structure colored by the  $\Delta$ HDX values; cold and warm colors indicate the HDX rates are higher and lower in T95D than WT, respectively.

Our previous reports indicated that the triangle formed by amino acids Trp3, Lys275, and Arg371, is essential for PVM binding (Lee et al., 2020; Saijo-Hamano

et al., 2021). Quite suggestively, we found that Trp3 and Arg371 in Irgb6-T95D-NF had flipped, changing the structure significantly compared with Irgb6-WT-NF.

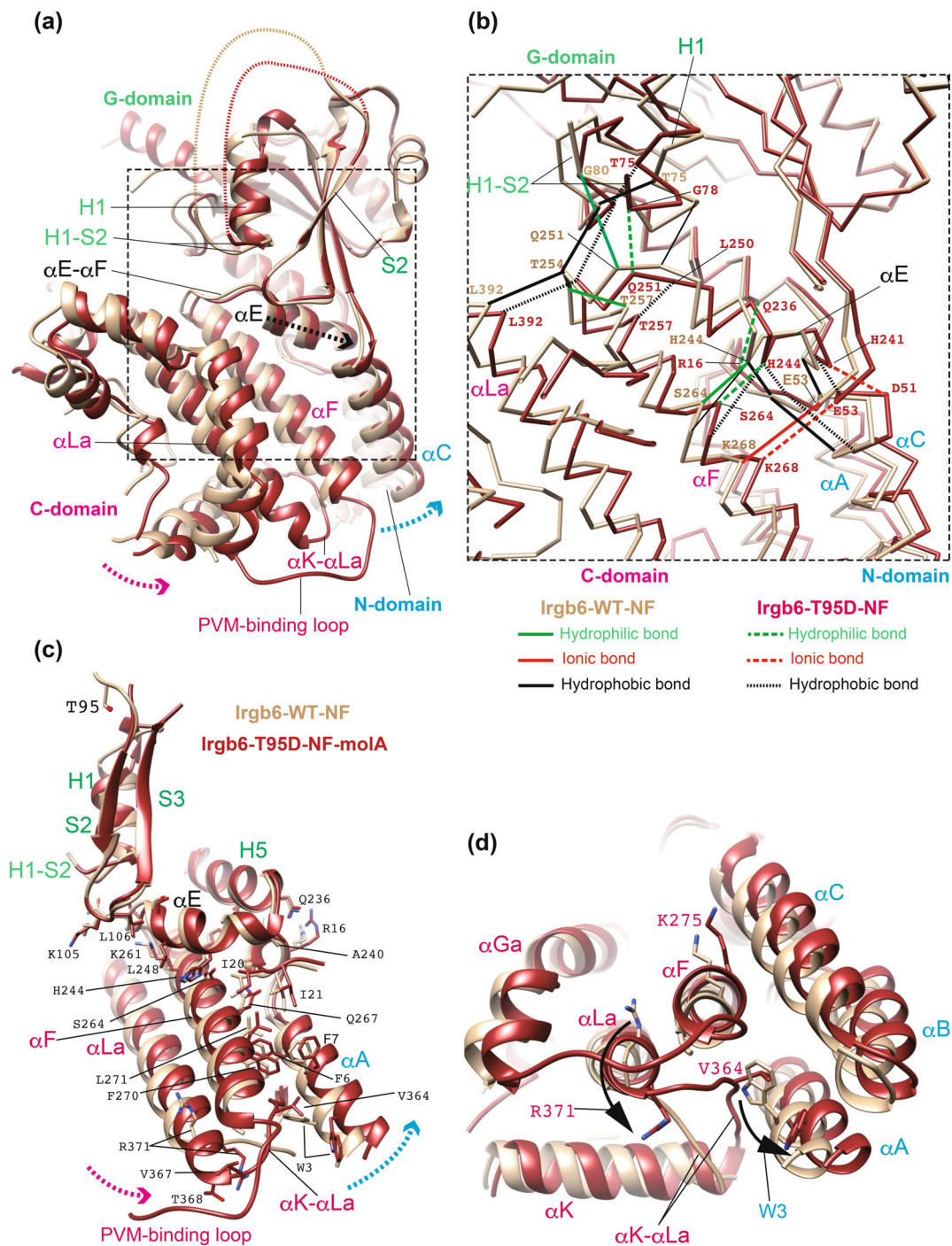


**FIGURE 7** T95D-induced conformational change in N- and C-domains. (a) Comparison of Irgb6-T95D-NF-molA (red) with Irgb6-WT-NF (light brown). (b) Changes of interdomain contacts by T95D mutation. Contacts among three domains and the helix  $\alpha E$  are shown in solid lines (Irgb6-WT-NF) and dotted lines (Irgb6-T95D-NF). Hydrophilic, ionic, and hydrophobic bonds are shown in green, red, and black. See Figure S5 for the overall view. (c) Transduction of conformational change from the active site in the G-domain to the N- and C-domains. (d) Conformational change of parasitophorous vacuole membrane (PVM) binding region. Flipping movements of Trp3 and Arg371 were observed. See Movie S1 for T95D-induced allosteric conformational change of Irgb6.

Accompanying this change were significant alterations in the conformation of the PVM-binding loop as well as the  $\alpha K$ - $\alpha La$  loop. These results suggest how, remarkably, the

structure of the membrane-binding interface of Irgb6 was significantly altered by the T95D mutation over 50 Å away.

## 2.6 | Phospholipid binding is drastically altered in Irgb6-T95D

Crystal structural analysis of Irgb6-T95D indicates that the T95D mutation dramatically changed the structure of the membrane-binding interface. Therefore, we examined the interaction between Irgb6 and the PI5P-containing PVM by molecular docking of the PI5P head group (PI5P: PubChem 643966) to the membrane-binding interface using Glide (Figure 8; Halgren et al., 2004). Since the whole structure of the PVM-binding loop was determined only in Irgb6-WT-GTP, Irgb6-T95D-GTP, and Irgb6-T95D-NF, the *in silico* docking of PI5P was performed using these structures as receptors. The grid box was approximately centered on residues Trp3, Lys275, and Arg371 of Irgb6-WT-GTP. We evaluated PI5P binding by the Glide scores, where a lower value indicates a more stable binding, and by the overall distribution of poses (Figure S8). To this end, we extracted all poses returned by Glide using default settings.

As previously reported, the head group of PI5P is bound to the region surrounded by Trp3, Lys275, and Arg371 in Irgb6-WT-GTP (Saijo-Hamano et al., 2021). The tips of the phosphate groups of PI5P were generally oriented to bind to Arg371 or Lys275 (Figure 8a). The tails of the head group generally pointed to the opposite side, implying that the acyl chain would extend toward the N-terminal helices. Another characteristic of Irgb6-WT-GTP is that the PI5P binding site was relatively broad. In the case of Irgb6-T95D-NF, on the other hand, PI5P was found to bind to a completely different location outside of the original binding site (Figure 8b,c). This alternative site is surrounded by R371 and Trp3, and thus this unusual pose was assumed to be due to the flipping of the side chains of these two amino acids. These results support the overall interpretation that the structural changes in the membrane-bound region induced by the T95D mutation impair the normal binding of PI5P-containing vesicles. We further discuss the alternative binding site produced in the Irgb6-T95D-NF below.

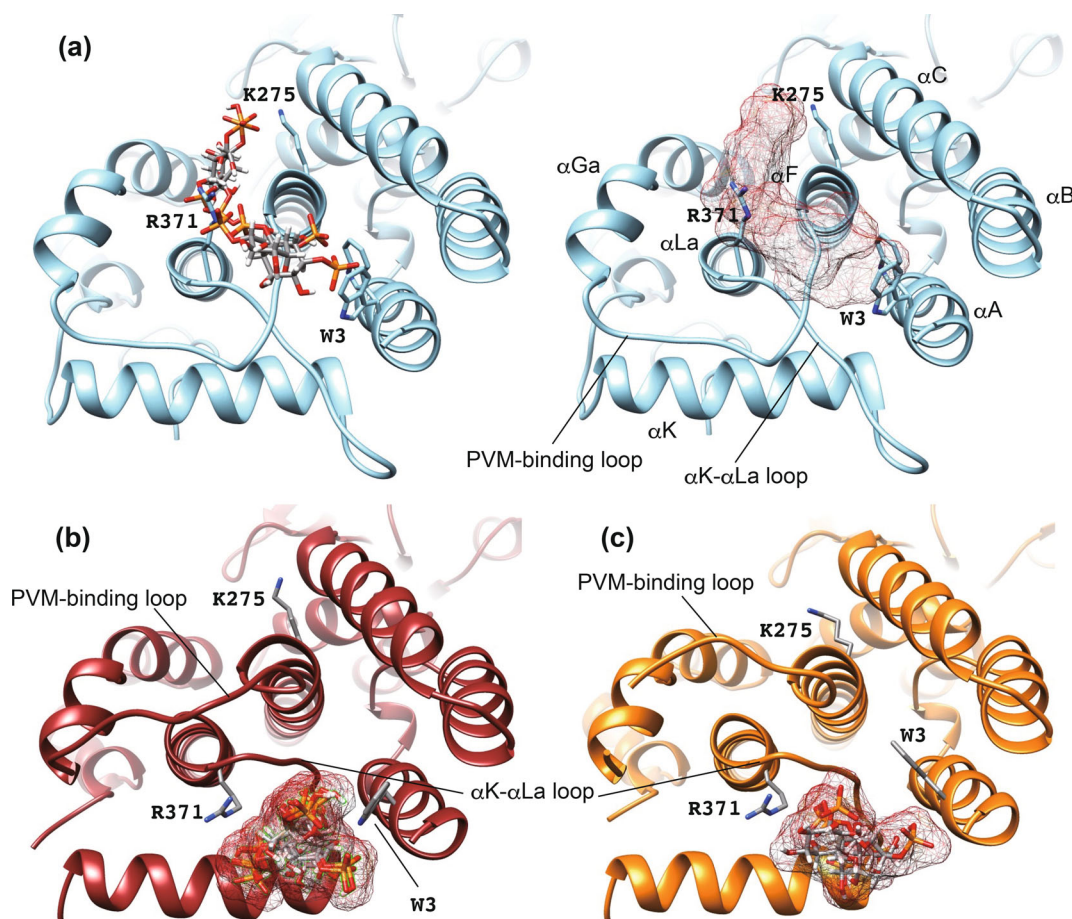


**FIGURE 8** *In silico* docking of PI5P to Irgb6-WT-GTP and Irgb6-T95D-NF. (a) *In silico* docking of PI5P head to the Irgb6-WT-GTP. Representative poses of PI5P are shown with the stick models (left) and with the molecular cloud (right). (b) *In silico* docking of PI5P head to the Irgb6-T95D-NF-molA. All poses of PI5P are overlaid. (c) *In silico* docking of PI5P head to the Irgb6-T95D-NF-molB. All poses of PI5P are overlaid.

### 3 | DISCUSSION

This study elucidated that infection with the low virulent type II *T. gondii* strongly induced phosphorylation of Thr95 of Irgb6. It has been known that ROP18 and ROP17 of the virulent type I *T. gondii* strongly inhibit the recruitment of IRGs to the PVM from the beginning of infection through the phosphorylation of switch I threonine residues of IRGs, including Thr95 in Irgb6 (Drewry et al., 2019; Fentress et al., 2010; Steinfeldt et al., 2010). In addition, the pseudokinase ROP5 and a dense granule protein GRA7 are involved in ROP17/ROP18-mediated IRG inactivation (Alaganan et al., 2014; Reese et al., 2014). However, the phosphorylation of Thr95 found in this study occurred after infection with type II *T. gondii* and the Irgb6 recruitment to the PVM. Currently, it is not clear whether this phosphorylation is mediated by a host or *T. gondii*. If deletion of ROP17 and/or ROP18 in type II *T. gondii* abrogates the Irgb6 phosphorylation, the ROP17/ROP18-dependent Irgb6 phosphorylation is an inactivation mechanism by *T. gondii*. It is also possible that the host cells may have their own inactivation system to terminate the IFN-inducible GTPase-dependent cell-autonomous immunity through the Irgb6 phosphorylation by host kinase(s). Further studies would clarify the contribution of the host and *T. gondii* to the Irgb6 inactivation in detail.

Structural studies found that the phosphomimetic mutation induces structural changes in the nucleotide-free state rather than in the GTP (or partly GDP) collision complex. Both biochemical and structural biological analyses also showed that Irgb6-T95D preserves GTP/GDP-binding ability, albeit the hydrolysis reaction rarely occurs in Irgb6-T95D (Figure 9a,b). Bound-GTP in Irgb6 in solution is trapped in the atypical position and away from switches I and II, even for Irgb6-WT (Figure S3; Saijo-Hamano et al., 2021). This conformation is caused by the Irgb6-specific G5 motif, reflecting the strict control for activating priming GTPase Irgb6; only after reaching the PVM, Irgb6-WT forms an oligomer effectively, inducing an isomerization reaction to change into the active Irgb6\*-GTP form. Irgb6-T95D further exhibited a reduced ability to form oligomers compared with Irgb6-WT. Thus, the basal GTPase rate of Irgb6-T95D is even slower than that of Irgb6-WT.

GTPase activation of Irgb6-T95D in the presence of a lipid membrane was not observed (Figure 3b). It is consistent with no recruitment of Irgb6-T95D to the PVM (Figure 2) and might be partly due to its low oligomerization activity if it could bind to the PVM. One matter of reference here is that the structure of Irgb6-T95D-NF differs significantly from that of Irgb6-WT-NF in both the oligomerization interface and the membrane-binding interface (Figure 9c,d).

Irgb6-T95D in solution or cytoplasm is thought to be in the equilibrium between the collision complex with GTP and the atypical nucleotide-free form. This equilibrium presumably tilts toward the GTP collision complex in cells with sufficiently high GTP concentrations. Therefore, it is still a matter of debate as to how the differences in the structure of the NF form are related to the inactivation of Irgb6-T95D. One possibility is that the isomerization reaction may only occur by passing through the physiological nucleotide-free form (Figure 9a,b). Further biochemical studies are awaited to prove this hypothesis.

The conformational change in Irgb6 induced by the T95D mutation is transmitted to linker helix  $\alpha$ E from the G-domain (H1 and H1-S2) and further converted into rotational movement of the helices in the N- and C-domains (Figure 7). Phospholipid binding sites are located at the border between the N- and C-domains, where Lys275 and Arg371 are involved in hydrophilic binding to phospholipids, and Trp3 is involved in hydrophobic binding. The Trp3 conformation affects the magnitude of the N- and C-terminal domain rotation angles (Figure S7). When the difference in rotation angle between the two domains increased by Trp3 flipping, a cleft was created between them, changing the conformation of the membrane binding interface. This is presumably a physiologically significant conformational change. Host cells and/or *T. gondii* efficiently utilize this strategy by phosphorylating only one threonine residue in the G-domain to open the cleft and disable the membrane binding interface.

By carrying out molecular docking, we detected an alternative binding site for PI5P in Irgb6-T95D because Arg371 and Trp3 flipped in the same direction in Irgb6-T95D. We preliminarily examined the Irgb6 binding to the PI5P-containing liposomes, albeit the binding affinity of both Irgb6-WT and T95D was not sufficiently high for the PI5P-containing liposomes to evaluate binding through the alternative binding site. The discrepancy between *in vitro* and *in-cell* experiments may come from the difference in posttranslational modifications because of the *Escherichia coli* expression system used, the composition of phospholipids, the curvature of the membrane, or the influence of other unknown factors in the cell, which should be clarified shortly. Since we performed the docking experiment using the PI5P head without acyl chains, it remains to be seen what happens when the acyl chains are attached and why Irgb6-T95D could not bind to the membrane *in vivo*. The other possibility remains that the alternative binding sites do not allow Irgb6-T95D to bind to the PVM in cells. Even if Irgb6-T95D can bind to the membrane through the alternative binding site, it may not accumulate as efficiently as the WT because it binds to the membrane as a

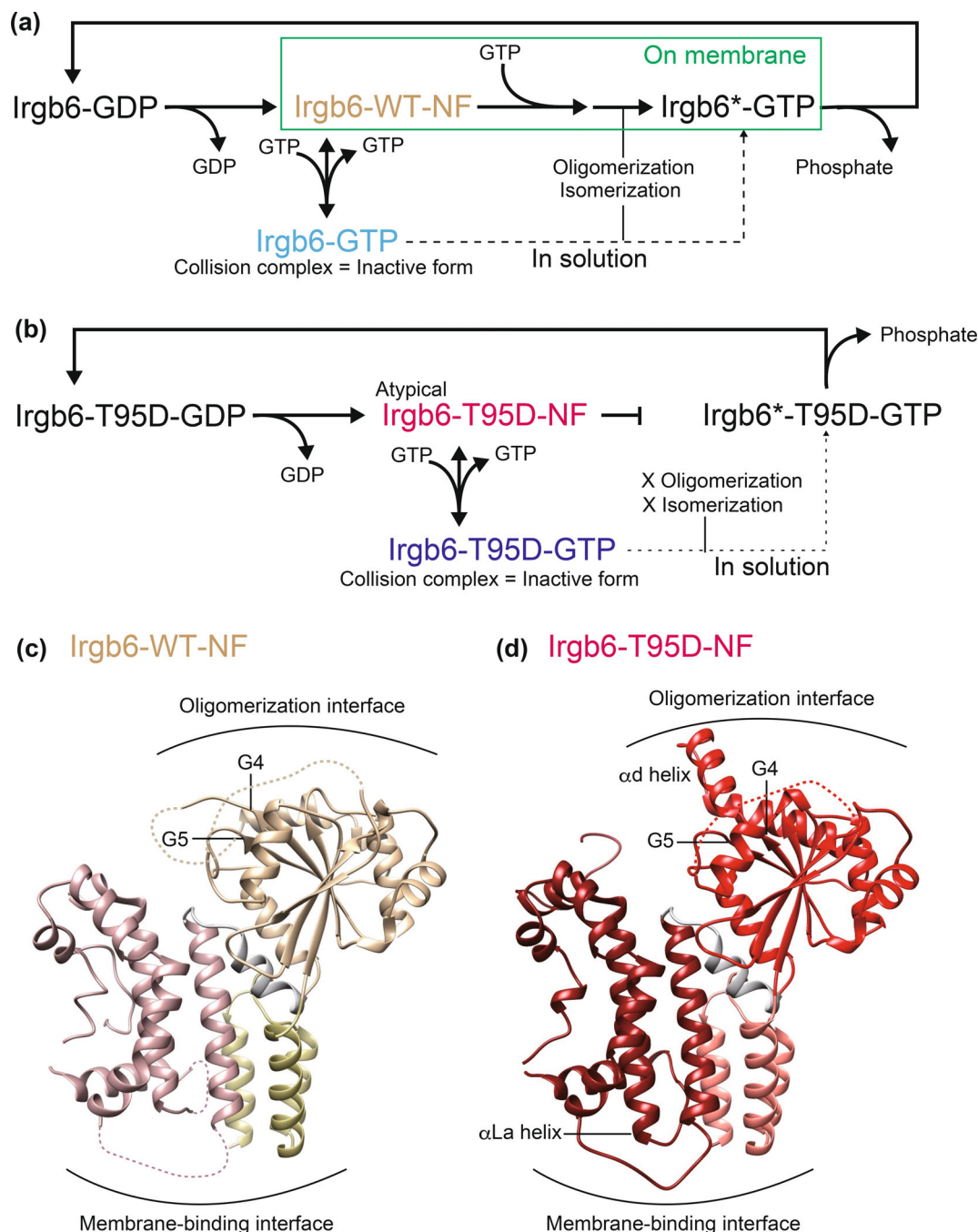


**FIGURE 9** The chemical cycle of Irgb6 GTPase. (a) The chemical cycle of wild-type Irgb6. Atomic structures of nucleotide-free Irgb6 (light brown; PDB ID 7VES) and Irgb6-GTP (light blue; PDB ID 7VEX) were reported previously (Saijo-Hamano et al., 2021). Membrane binding and/or oligomerization may stimulate the isomerization step and/or hydrolysis step. (b) The chemical cycle of Irgb6-T95D. Atomic structures of nucleotide-free Irgb6-T95D (red) and Irgb6-T95D-GTP (blue) were solved here. The phosphomimetic mutation T95D inhibits the isomerization reaction of Irgb6. (c,d) The oligomerization and membrane-binding interfaces of Irgb6-WT-NF (c) and Irgb6-T95D-NF (d). These interfaces show major conformational changes, including the loop-to-helix transition of  $\alpha$ d helix or the elongation of  $\alpha$ La helix.

monomer. Additionally, PI5P-binding sites were relatively broadly distributed in the wild-type Irgb6, whereas Irgb6-T95D has a quite narrow alternative binding site. The physiological significance of these distinct binding patterns awaits further structural analysis of membrane-bound Irgb6.

## 4 | EXPERIMENTAL PROCEDURES

### 4.1 | Reagents

Antibodies against FLAG M2 (F3165) were purchased from Sigma. Mouse monoclonal anti-p62 (PM045)

antibody was obtained from MBL International. Anti-ubiquitin mouse monoclonal antibody (FK2; MFK-004) was obtained from NIPPON BIOTEST LABORATORIES. Mouse monoclonal anti-Irga6 (10D7) and rabbit polyclonal anti-Irgb10 antibodies were kindly provided by Dr. J. C. Howard (Instituto Gulbenkian de Ciência). Rabbit polyclonal anti-GRA7 antibody was kindly provided by Dr. J. C. Boothroyd (Stanford University School of Medicine). Mouse monoclonal anti-GRA2 antibody was kindly provided by Dr. D. Soldati-Favre (University of Geneva). Recombinant mouse IFN- $\gamma$  was obtained from PeproTech.

## 4.2 | Reconstitution of Irgb6 in Irgb6-deficient MEFs

Irgb6-deficient MEFs were previously generated (Lee et al., 2020), and maintained in DMEM (Nacalai Tesque) supplemented with 10% heat-inactivated fetal bovine serum (FBS; JRH Bioscience), 100 U/mL penicillin (Nacalai Tesque), and 100  $\mu$ g/mL streptomycin (Nacalai Tesque). The Irgb6 T95D mutant was generated using the plasmid pRN203 described below and PCR-amplified using primers (5'-gaattcaccATGGCTTGGGCCTCCAGC TTTGA -3' and 5'-gcccgcctactcagAGCTTCCAG-TACTCGGGGGGCTCA -3'). The PCR product was then ligated into the retroviral pMRX expression vector for retroviral infection. The sequence of all constructs was confirmed by DNA sequencing.

## 4.3 | Immunofluorescence assay

MEFs were plated at equal densities ( $1.5 \times 10^5$  cells per well in a 6-well plate) on glass coverslips and exposed to 10 ng/mL IFN- $\gamma$  for 18–20 h at 37°C. The cells were infected with ME49 tachyzoites at MOI 4 and incubated at 37°C for 2 h. Next, cells were fixed in PBS containing 3.7% paraformaldehyde for 10 min. Cells were then permeabilized with 0.002% digitonin in PBS for 10 min and blocked with 8% FBS in PBS for 10 min.

Cells were costained with anti-GRA7 rabbit antibody and anti-Flag, Irga6, Ubiquitin, p62 mouse antibodies for 1 h, followed by incubation with Alexa 488-conjugated antirabbit and Alexa 594-conjugated antimouse secondary antibodies and DAPI for 30 min in the dark. Coverslips were mounted onto glass slides with PermaFluor and analyzed with confocal laser microscopy (Olympus FV3000 IX83). All procedures following 2 h incubation were done in room temperature. All images were taken with a 60 $\times$  objective lens.

## 4.4 | Mass spectrometry analysis

Irgb6-deficient MEFs stably expressing Spot-tagged Irgb6 were infected with or without *T. gondii* ME49 for 4 h and lysed in guanidine buffer (6 M guanidine-HCl, 100 mM Tris-HCl, pH 8.0, and 2 mM DTT). The lysates were diluted 8-fold with RIPA buffer (20 mM HEPES-NaOH, pH 7.5, 150 mM NaCl, 1 mM EGTA, 1 mM MgCl<sub>2</sub>, 0.25% sodium deoxycholate, 0.05% SDS, and 1% NP-40) supplemented with cOmplete protease inhibitor cocktail and PhosSTOP phosphatase inhibitor cocktail (Roche). After centrifugation at 20,000  $\times$  g for 15 min at 4°C, the supernatants were incubated with a 5- $\mu$ L slurry of anti-Spot nanobody-coupled magnetic agarose beads (Spot-Trap, ChromoTek) for 3 h at 4°C. The beads were washed four times with RIPA buffer and then twice with 50 mM ammonium bicarbonate. Proteins on the beads were digested with 200 ng trypsin (MS grade, Thermo Fisher Scientific) at 37°C overnight. The digests were reduced, alkylated, acidified, and desalted using GL-Tip SDB (GL Sciences). The eluates were evaporated and dissolved in 3% acetonitrile (ACN) and 0.1% trifluoroacetic acid. LC-MS/MS analysis of the resultant peptides was performed on an EASY-nLC 1200 UHPLC connected to a Q Exactive Plus mass spectrometer through a nano-electrospray ion source (Thermo Fisher Scientific). The peptides were separated on a 75- $\mu$ m inner diameter  $\times$  150 mm C18 reversed-phase column (Nikkyo Technos) with a linear 4%–32% ACN gradient for 0–100 min, followed by an increase to 80% ACN for 10 min and finally held at 80% ACN for 10 min. The mass spectrometer was operated in data-dependent acquisition mode with the top 10 MS/MS method. MS1 spectra were measured with a resolution of 70,000, an automatic gain control target of 1e6, and a mass range from 350 to 1500 *m/z*. HCD MS/MS spectra were acquired at a resolution of 17,500, an automatic gain control target of 5e4, an isolation window of 2.0 *m/z*, a maximum injection time of 60 ms, and a normalized collision energy of 27. Dynamic exclusion was set to 20 s. Raw data were directly analyzed against the SwissProt database restricted to *Mus musculus* supplemented with amino acid sequences of Spot-tagged Irgb6 and *T. gondii* ME49 proteins (ToxoDB release 38) using Proteome Discoverer v2.5 (Thermo Fisher Scientific) with the Sequest HT search engine. The search parameters were as follows: (a) trypsin as an enzyme with up to two missed cleavages; (b) precursor mass tolerance of 10 ppm; (c) fragment mass tolerance of 0.02 Da; (d) carbamidomethylation of cysteine as a fixed modification; (e) acetylation of the protein N-terminus, oxidation of methionine, and phosphorylation of serine, threonine, and tyrosine as variable modifications. Peptides were

filtered at a false discovery rate of 1% using the Percolator node.

#### 4.5 | Protein expression and purification

To create a GST-tagged Irgb6-T95D expression plasmid (pRN203), a pRN108 plasmid which is a GST-tagged Irgb6-WT expression plasmid (Sasai et al., 2018) was PCR-amplified with specific primers (5'-CCACTGGC GCAATAGAGACAGATATGAAGAGAACTCCA-3' and 5'-TGTCTCTATTGCGCCAGTGG -3'; the original sequence of pRN108 is underlined), and then ligated by Hi-Fi DNA assembly (New England Biolabs Inc.). Irgb6-WT and Irgb6-T95D were expressed and purified as described (Saijo-Hamano et al., 2021). Briefly, a protein expressed in *E. coli* BL21(DE3) was purified by affinity chromatography using Glutathione Sepharose 4B column (Cytiva) and treated with GST-tagged HRV 3C protease (homemade) on the resin. The free protein was further purified by SEC using a HiLoad 16/600 Superdex 75 column pg column (Cytiva).

#### 4.6 | Analysis of nucleotide component

The nucleotide component by GTPase activity was analyzed as described (Saijo-Hamano et al., 2021). The protein sample and GTP were prepared in 200  $\mu$ M in 50 mM HEPES-KOH, pH 7.5, 1 mM MgCl<sub>2</sub>, 1 mM EGTA-KOH, pH 7.0, and 150 mM NaCl. A 25  $\mu$ L Irgb6 sample was mixed with an equal volume of GTP sample and incubated at 37°C for 30 min. A 1 mL of 8 M urea was added to the mixture and heated at 95°C for 1 min, followed by ultrafiltration using Amicon Ultra-0.5 10-kD MWCO concentrator (Merck Millipore). A 900  $\mu$ L of the solution that passed through the ultrafiltration membrane was analyzed by anion exchange chromatography using a Mono Q 5/50 GL column (Cytiva) equilibrated with 50 mM HEPES-KOH, pH 7.0. Components of the reaction mixture, GTP and GDP, were completely separated by elution with 0–0.2 M NaCl gradient in 50 mM HEPES-KOH, pH 7.0. Fresh GTP (Nacalai Tesque) and GDP (WAKO) were used to confirm the elution position. A control experiment was performed using the reaction buffer.

#### 4.7 | Guanine nucleotide-binding affinity measurement

The guanine nucleotide-binding affinities were measured by means of equilibrium titration using 2'/3'-O-(N-

methyl-anthraniloyl) (Mant)-labeled nucleotide analogs (Jena Bioscience). Purified Irgb6-WT or Irgb6-T95D was titrated, in a range from 0 to 80  $\mu$ M, to 0.5  $\mu$ M Mant-GDP or Mant-GTP $\gamma$ S, in 50 mM Tris-HCl (pH 7.4), 5 mM MgCl<sub>2</sub>, 2 mM DTT at 25°C. The fluorescence of Mant-nucleotides, excited at 355 nm, was monitored at 422 nm using FP-8200 fluorescence spectrometer (JASCO). The equilibrium dissociation constants ( $K_d$ ) were calculated by fitting a quadratic function described by Herrmann and Nassar (Herrmann & Nassar, 1996) using Kaleida-Graph (Synergy Software Inc.).

#### 4.8 | Preparation for liposomes

Liposomes were prepared as previously described (Yamada et al., 2022). Ten percent (mol/mol) phosphatidylinositol-5-phosphate (PI5P; Cat no. P-5016, Echelon Biosciences), 80% phosphatidylethanolamine (PE; Cat no. 840022C, Avanti Polar Lipids), 10% cholesterol (Chol; Cat no. 700000, Avanti Polar Lipids) were mixed in chloroform-methanol mixture (1:3 v/v). The lipids (250 mg) were taken in glass tubes, and the solvent was evaporated using slow-flow nitrogen gas to produce a lipid film and then completely dried under vacuum for 1 day. The lipid film was rehydrated by passing water-saturated nitrogen gas, followed by the addition of 250  $\mu$ L of filtered 0.3 M sucrose, then left to stand for 2 h at 37°C. The resultant liposomes were passed through polycarbonate filters with 0.4  $\mu$ m pore 11 times using Avanti Mini extruder. The liposomes were stored at 4°C until use.

#### 4.9 | GTPase assay

To determine the PI5P-stimulated GTPase activity, 20  $\mu$ M Irgb6-WT or Irgb6-T95D in 100 mM NaCl, 2 mM MgCl<sub>2</sub>, 1 mM DTT, 20 mM HEPES-NaOH, pH 7.5 was preincubated for 5 min at 25°C. The reaction was started by adding 1 mM GTP in the presence or absence of 0.1 mg/mL PI5P-containing liposomes, and further incubated at 37°C for 15 min. The GTPase reaction was stopped by adding 0.1 M EDTA. GTP hydrolysis in 16  $\mu$ L of the reaction mixture was measured using a colorimetric assay to detect inorganic phosphate (Pi) release as previously described (Leonard et al., 2005).

For the GTPase assay under low ionic- or high ionic-strength conditions, 20  $\mu$ M Irgb6-WT or Irgb6-T95D was dissolved in 2 mM MgCl<sub>2</sub>, 1 mM DTT, 2 mM EGTA, 20 mM HEPES-KOH, pH 7.5 (Low ionic strength buffer), or in 100 mM NaCl, 2 mM MgCl<sub>2</sub>, 1 mM DTT, 2 mM EGTA, 20 mM HEPES-NaOH, pH 7.5 (high ionic

strength buffer), respectively. The mixture was preincubated at 25°C for 5 min. The reaction was started by adding 1 mM GTP and incubated at 37°C for 30, 60, and 120 min. The GTP hydrolysis in 16  $\mu$ L of the reaction mixture was measured using a colorimetric assay as described above.

Data were analyzed for statistical significance using Kaleida Graph software for Macintosh, version 5.04 (Synergy Software Inc.). Student's *t*-tests were used to analyze the statistical significance between the two groups. All data are displayed as means  $\pm$  standard error of the means (SEM) with *p* < .05 considered statistically significant.

#### 4.10 | MP experiments

According to the manufacturer's operation manual, MP measurements were conducted using a TwoMP mass photometer (Refeyn Japan K.K.). A precleaned coverslip and gasket (Refeyn Japan K.K.) were assembled and positioned onto the mass photometer. Contrast-to-mass calibration was conducted using purified bovine serum albumin and apoferritin proteins. Focal calibration was established using the incubation buffer (20 mM HEPES-KOH, pH 7.5, 100 mM NaCl, 2 mM MgCl<sub>2</sub>, 1 mM DTT) in the absence or presence of GDP-Pi (1 mM GDP, 5 mM NaF, 0.5 mM AlCl<sub>3</sub>) corresponding to each sample. Either Irgb6-WT or Irgb6-T95D at a concentration of 5  $\mu$ M was preincubated in the absence or presence of GDP-Pi at 37°C for 20 min. Subsequently, 0.5  $\mu$ L of the sample was added to 99.5  $\mu$ L of the same incubation buffer on a coverslip, resulting in a final concentration of  $\sim$ 25 nM. After achieving autofocus stabilization, MP videos were recorded for 40 s. Each recorded contrast distribution was fitted to a Gaussian curve employing the maximum-likelihood procedure. These measurements were then converted into mass values using the established contrast-to-mass calibration.

#### 4.11 | Nucleotide-dependent Irgb6 polymer formation

Irgb6-WT or Irgb6-T95D at 5  $\mu$ M in 100 mM NaCl, 2 mM MgCl<sub>2</sub>, 1 mM DTT, 20 mM HEPES-NaOH, pH 7.5 at 37°C for 15 min in the presence or absence of 5 mM GMP-PNP (Cat no. G0635, Sigma-Aldrich). To make the GDP-Pi binding state of Irgb6, 0.9 mM GDP, 4.5 mM NaF, and 0.45 mM AlCl<sub>3</sub> were added to the protein solution. The samples were absorbed onto a Formvar- and carbon-coated copper grid (company) and were incubated

for 5 min. The samples on grids were negative-stained with 3% uranyl acetate in double deionized H<sub>2</sub>O for 2 min and observed with a transmission electron microscope (H-7650, Hitachi High-Tech Corp.) at a voltage of 120 kV.

#### 4.12 | Crystallization

Irgb6-T95D was concentrated to 8 mg/mL in SEC solution consisting of 20 mM Tris-HCl pH 7.5 (WAKO), 5 mM MgCl<sub>2</sub> (WAKO), 150 mM NaCl (Nacalai Tesque), and 2 mM dithiothreitol (Nacalai Tesque). Protein concentration was estimated by assuming an A280 nm of 0.916 for a 1 mg/mL solution. Nucleotide-free Irgb6-T95D crystals diffracting to 2.05 Å resolution were obtained from sitting drops with a 0.5  $\mu$ L of protein solution and a 0.5  $\mu$ L of reservoir solution consisting of 0.2 M Sodium malonate pH 7.0 (Molecular Dimensions), 20% Polyethylene Glycol 3350 (Molecular Dimensions) at 20°C. GTP-binding Irgb6-T95D crystals diffracting to 1.68 Å resolution were obtained from sitting drops with a 0.5  $\mu$ L of protein solution containing 2 mM GTP (Roche) and a 0.5  $\mu$ L of reservoir solution consisting of 0.2 M Sodium sulfate (Molecular Dimensions) and 20% (w/v) polyethylene glycol 3350 (Molecular Dimensions) at 20°C.

#### 4.13 | Data collection and structure determination

Single crystals were mounted in LithoLoops (Protein Wave) with the mother liquor containing 10% (v/v) glycerol as a cryoprotectant and were frozen directly in liquid nitrogen before x-ray experiments. Diffraction data collection was performed on the BL32XU beamline at SPring-8 using the automatic data collection system ZOO (Hirata et al., 2019). The diffraction data were processed and scaled using the automatic data processing pipeline KAMO (Yamashita et al., 2018). The structure was determined using PHENIX software suite (Liebschner et al., 2019). Initial phase was solved by molecular replacement using the Irgb6-WT crystal models (PDB ID: 7VES and 7VEX) with phenix.phaser. The initial model was automatically constructed with phenix.AutoBuild. The model was manually built with Coot (Emsley & Cowtan, 2004) and refined with phenix.refine. The statistics of the data collection and the structure refinement are summarized in Table 1. UCSF Chimera (Pettersen et al., 2004) was used to create images and compare structures.

## 4.14 | Hydrogen-deuterium exchange mass spectrometry

The protein was dispensed in a vial as 1 mg/mL in Tris-HCl buffer (20 mM Tris-HCl, pH 7.5, 5 mM MgCl<sub>2</sub>, 150 mM NaCl). GTP was added to the protein solution at a final concentration of 1 mM. The HDX experiment was performed by the Traijan HDX system with Cronos software. The HDX condition was as follows: 2 μL protein solution was diluted into the 28 μL of Tris-HCl buffer consisting of 100% H<sub>2</sub>O or 90% D<sub>2</sub>O with/without indicated incubation timing. After the incubation timing, the diluted protein solution was quenched with 30 μL of a buffer consisting of 2 M Guanidine hydrochloride, 100 mM citrate in 0.1% formic acid water, then injected into the online digestion column, ProDx Protease column with 0.1% formic acid water flow rate at 1 μL/min for 3 min.

The digested products were trapped by GL Science Intersil Sulfa C18 guard column 1.0 × 10 mm for 1 min, then, eluted and separated by Thermo Scientific Hypersil GOLD C18 2.1 × 50 mm column.

Analytical column flow was controlled by Agilent 1290 HPLC pump with mobile phase A: 0.1% formic acid water and B: 0.1% formic acid ACN. The analytical elution gradient was set as 5%B to 40%B in 20 min. tims TOF Pro (Bruker) was used for mass spectrometry with the following condition: ESI ion source was used, a capillary voltage was 4500 V, dry gas 4.5 L/min, scan range from 350 to 2000 *m/z*. MS2 was conducted for peptide identification, and MS measurements were conducted for nondeuterium and deuterium labeling experiments. The peptide identification was processed by PEAKS StudioX with no enzyme digestion condition, and H-D exchange data were analyzed by HDXaminer.

## 4.15 | In situ docking simulation

### 4.15.1 | Protein structure preparation

The *Protein preparation wizard* from Schrödinger suite (Sastry et al., 2013) was used to prepare Irgb6-WT-GTP and Irgb6-T95D in GTP-bound and nucleotide-free protein structures using default parameters. There were two positions for Trp3 with average occupancies of 0.53 and 0.47. Protein structures with each Trp3 position were generated. Since the Incorporation of active site water molecules in the docking process is challenging (Elokely & Doerksen, 2013), protein structures with and without water were generated. In addition, protein struc-

tures with the Arg371 sidechain remodeled by Scwrl4 (Krivov et al., 2009) were prepared for each protein structure. Thus, for each protein, eight structures were docked (TRPA/B × Water/NoWater × ARG371Remodeled/Not-Modeled). The Grid box was centered on the midpoint of Trp3, Lys275 and Arg371 using *receptor grid generation* from Schrödinger suite. The protein grids were 20 × 20 × 20 Å in size. Eight grids were generated for the eight structures.

### 4.15.2 | Ligand preparation

The Pi5P molecule was truncated up to the polar head before being prepared.

*LigPrep* from Schrödinger suite was used to produce low-energy, three-dimensional ligands with correct chirality. Three conformations were generated and used for docking.

### 4.15.3 | Molecular docking

The three Pi5P head conformations were docked to the eight grids using *Glide* (Grid-based Ligand Docking with Energetics) from the Schrödinger suite. *Glide* measures the ligand-receptor binding affinity in terms of *Glide* score. For Irgb6-T95D-NF protein, Pi5P was docked to each chain separately. In this study, since we were focused on the global pattern of ligand distribution around the active site of the protein, and used all ligand poses, selected by *Glide* (usually 2–3 per docking run).

## AUTHOR CONTRIBUTIONS

Conceptualization: Hiromichi Okuma, Yumiko Saijo-Hamano, Masahiro Yamamoto, and Ryo Nitta. Methodology: Yumiko Saijo-Hamano, Naoki Sakai, Hidetaka Kosako, Daron M. Standley, and Masahiro Yamamoto. Investigation: Hiromichi Okuma, Yumiko Saijo-Hamano, Hiroshi Yamada, Aalaa Alrahman Sherif, Emi Hashizaki, Naoki Sakai, Takaaki Kato, Tsuyoshi Imasaki, Satoshi Kikkawa, Eriko Nitta, Miwa Sasai, Tadashi Abe, Fuminori Sugihara, Hidetaka Kosako, and Daron M. Standley. Supervision: Yoshimasa Maniwa, Hidetaka Kosako, Kohji Takei, Daron M. Standley, Masahiro Yamamoto, Ryo Nitta. Writing—original draft: Hiromichi Okuma, Yumiko Saijo-Hamano, Hiroshi Yamada, Aalaa Alrahman Sherif, Hidetaka Kosako, Daron M. Standley, Masahiro Yamamoto, and Ryo Nitta. Writing—review and editing: Hidetaka Kosako, Kohji Takei, Daron M. Standley, Masahiro Yamamoto, and Ryo Nitta.

## ACKNOWLEDGMENTS

We thank K. Chin, T. Setsu, Y. Sakihama, and T. Shimizu for assistance and other colleagues for discussions. We also thank Dr. Kohei Nishino for technical assistance in LC-MS/MS analysis and Dr. Daisuke Miyoshi and Mr. Yoshiki Hashimoto at Konan University FIRST for technical assistance in the equilibrium titration experiments for guanine nucleotide-binding analysis. This research was partially supported by Platform Project for Supporting Drug Discovery and Life Science Research (Basis for Supporting Innovative Drug Discovery and Life Science Research [BINDS]) from AMED under Grant Number JP21am0101070.

## FUNDING INFORMATION

Japan Agency for Medical Research and Development (AMED) (JP23fk0108682, JP22wm0325010, JP223fa627002 to MY; JP20am0101108 to DMS; JP21gm0810013 to RN). Japan Society for the Promotion of Science (21K06988 to YS-H; 20B304, 19H04809, 19H00970 to MY; 21H05254, 21K19352, 22H02795 to RN). Japan Science and Technology Agency (Moonshot R&D; JPMJMS2024 to RN).

## CONFLICT OF INTEREST STATEMENT

All other authors declare they have no competing interests.

## ORCID

Ryo Nitta  <https://orcid.org/0000-0002-6537-9272>

## REFERENCES

- Alaganan, A., Fentress, S. J., Tang, K., Wang, Q., & Sibley, L. D. (2014). Toxoplasma GRA7 effector increases turnover of immunity-related GTPases and contributes to acute virulence in the mouse. *Proceedings of the National Academy of Sciences of the United States of America*, *111*, 1126–1131. <https://doi.org/10.1073/pnas.1313501111>
- Behnke, M. S., Fentress, S. J., Mashayekhi, M., Li, L. X., Taylor, G. A., & Sibley, L. D. (2012). The polymorphic pseudokinase ROP5 controls virulence in *Toxoplasma gondii* by regulating the active kinase ROP18. *PLoS Pathogens*, *8*, e1002992. <https://doi.org/10.1371/journal.ppat.1002992>
- Behnke, M. S., Khan, S., Wootton, J. C., Dubey, J. P., Tang, K., & Sibley, L. D. (2011). Virulence differences in toxoplasma mediated by amplification of a family of polymorphic pseudokinases. *Proceedings of the National Academy of Sciences of the United States of America*, *108*, 9631–9636. <https://doi.org/10.1073/pnas.1015338108>
- Boothroyd, J. C. (2009). *Toxoplasma gondii*: 25 years and 25 major advances for the field. *International Journal for Parasitology*, *39*, 935–946. <https://doi.org/10.1016/j.ijpara.2009.02.003>
- Bourne, H. R., Sanders, D. A., & McCormick, F. (1990). The GTPase superfamily: A conserved switch for diverse cell functions. *Nature*, *348*, 125–132. <https://doi.org/10.1038/348125a0>
- Divanovic, S., Sawtell, N. M., Trompette, A., Warning, J. I., Dias, A., Cooper, A. M., Yap, G. S., Ardit, M., Shimada, K., DuHadaway, J. B., Prendergast, G. C., Basaraba, R. J., Mellor, A. L., Munn, D. H., Aliberti, J., & Karp, C. L. (2012). Opposing biological functions of tryptophan catabolizing enzymes during intracellular infection. *The Journal of Infectious Diseases*, *205*, 152–161. <https://doi.org/10.1093/infdis/jir621>
- Drewry, L. L., Jones, N. G., Wang, Q., Onken, M. D., Miller, M. J., & Sibley, L. D. (2019). The secreted kinase ROP17 promotes *Toxoplasma gondii* dissemination by hijacking monocyte tissue migration. *Nature Microbiology*, *4*, 1951–1963. <https://doi.org/10.1038/s41564-019-0504-8>
- Elokely, K. M., & Doerksen, R. J. (2013). Docking challenge: Protein sampling and molecular docking performance. *Journal of Chemical Information and Modeling*, *53*, 1934–1945. <https://doi.org/10.1021/ci400040d>
- Emsley, P., & Cowtan, K. (2004). Coot: Model-building tools for molecular graphics. *Acta Crystallographica. Section D: Biological Crystallography*, *60*, 2126–2132. <https://doi.org/10.1107/S0907444904019158>
- Etheridge, R. D., Alaganan, A., Tang, K., Lou, H. J., Turk, B. E., & Sibley, L. D. (2014). The toxoplasma pseudokinase ROP5 forms complexes with ROP18 and ROP17 kinases that synergize to control acute virulence in mice. *Cell Host & Microbe*, *15*, 537–550. <https://doi.org/10.1016/j.chom.2014.04.002>
- Fentress, S. J., Behnke, M. S., Dunay, I. R., Mashayekhi, M., Rommereim, L. M., Fox, B. A., Bzik, D. J., Taylor, G. A., Turk, B. E., Lichti, C. F., Townsend, R. R., Qiu, W., Hui, R., Beatty, W. L., & Sibley, L. D. (2010). Phosphorylation of immunity-related GTPases by a *Toxoplasma gondii* secreted kinase promotes macrophage survival and virulence. *Cell Host & Microbe*, *8*, 484–495. <https://doi.org/10.1016/j.chom.2010.11.005>
- Goldstein, E. J. C., Montoya, J. G., & Remington, J. S. (2008). Management of *Toxoplasma gondii* infection during pregnancy. *Clinical Infectious Diseases*, *47*, 554–566. <https://doi.org/10.1086/590149>
- Haldar, A. K., Foltz, C., Finethy, R., Piro, A. S., Feeley, E. M., Pilla-Moffett, D. M., Komatsu, M., Frickel, E. M., & Coers, J. (2015). Ubiquitin systems mark pathogen-containing vacuoles as targets for host defense by guanylate binding proteins. *Proceedings of the National Academy of Sciences of the United States of America*, *112*, E5628–E5637. <https://doi.org/10.1073/pnas.1515966112>
- Halgren, T. A., Murphy, R. B., Friesner, R. A., Beard, H. S., Frye, L. L., Pollard, W. T., & Banks, J. L. (2004). Glide: A new approach for rapid, accurate docking and scoring. 2. Enrichment factors in database screening. *Journal of Medicinal Chemistry*, *47*, 1750–1759. <https://doi.org/10.1021/jm030644s>
- Herrmann, C., & Nassar, N. (1996). Ras and its effectors. *Progress in Biophysics and Molecular Biology*, *66*, 1–41. [https://doi.org/10.1016/S0079-6107\(96\)00015-6](https://doi.org/10.1016/S0079-6107(96)00015-6)
- Hirata, K., Yamashita, K., Ueno, G., Kawano, Y., Hasegawa, K., Kumasaka, T., & Yamamoto, M. (2019). ZOO: An automatic data-collection system for high-throughput structure analysis in

- protein microcrystallography. *Acta Crystallographica Section D: Structural Biology*, 75, 138–150. <https://doi.org/10.1107/S2059798318017795>
- Howard, J. C., Hunn, J. P., & Steinfeldt, T. (2011). The IRG protein-based resistance mechanism in mice and its relation to virulence in *Toxoplasma gondii*. *Current Opinion in Microbiology*, 14, 414–421. <https://doi.org/10.1016/j.mib.2011.07.002>
- Hunn, J. P., Koenen-Waisman, S., Papic, N., Schroeder, N., Pawlowski, N., Lange, R., Kaiser, F., Zerrahn, J., Martens, S., & Howard, J. C. (2008). Regulatory interactions between IRG resistance GTPases in the cellular response to *Toxoplasma gondii*. *The EMBO Journal*, 27, 2495–2509. <https://doi.org/10.1038/emboj.2008.176>
- Khaminets, A., Hunn, J. P., Konen-Waisman, S., Zhao, Y. O., Preukschat, D., Coers, J., Boyle, J. P., Ong, Y. C., Boothroyd, J. C., Reichmann, G., & Howard, J. C. (2010). Coordinated loading of IRG resistance GTPases on to the *Toxoplasma gondii* parasitophorous vacuole. *Cellular Microbiology*, 12, 939–961. <https://doi.org/10.1111/j.1462-5822.2010.01443.x>
- Kim, B. H., Shenoy, A. R., Kumar, P., Bradfield, C. J., & MacMicking, J. D. (2012). IFN-inducible GTPases in host cell defense. *Cell Host & Microbe*, 12, 432–444. <https://doi.org/10.1016/j.chom.2012.09.007>
- Krivov, G. G., Shapovalov, M. V., & Dunbrack, R. L., Jr. (2009). Improved prediction of protein side-chain conformations with SCWRL4. *Proteins*, 77, 778–795. <https://doi.org/10.1002/prot.22488>
- Lee, Y., Sasai, M., Ma, J. S., Sakaguchi, N., Ohshima, J., Bando, H., Saitoh, T., Akira, S., & Yamamoto, M. (2015). p62 plays a specific role in interferon- $\gamma$ -induced presentation of a toxoplasma vacuolar antigen. *Cell, Rep.* 13, 223–233. <https://doi.org/10.1016/j.celrep.2015.09.005>
- Lee, Y., Yamada, H., Pradipta, A., Ma, J. S., Okamoto, M., Nagaoka, H., Takashima, E., Standley, D. M., Sasai, M., Takei, K., & Yamamoto, M. (2020). Initial phospholipid-dependent Irgb6 targeting to *Toxoplasma gondii* vacuoles mediates host defense. *Life Science Alliance*, 3, e201900549. <https://doi.org/10.26508/lsa.201900549>
- Leonard, M., Song, B. D., Ramachandran, R., & Schmid, S. L. (2005). Robust colorimetric assays for dynamin's basal and stimulated GTPase activities. *Methods in Enzymology*, 404, 490–503. [https://doi.org/10.1016/S0076-6879\(05\)04043-7](https://doi.org/10.1016/S0076-6879(05)04043-7)
- Liebschner, D., Afonine, P. V., Baker, M. L., Bunkoczi, G., Chen, V. B., Croll, T. I., Hintze, B., Hung, L. W., Jain, S., McCoy, A. J., Moriarty, N. W., Oeffner, R. D., Poon, B. K., Prisant, M. G., Read, R. J., Richardson, J. S., Richardson, D. C., Sammito, M. D., Sobolev, O. V., ... Adams, P. D. (2019). Macromolecular structure determination using X-rays, neutrons and electrons: Recent developments in phenix. *Acta Crystallographica Section D: Structural Biology*, 75, 861–877. <https://doi.org/10.1107/S2059798319011471>
- MacMicking, J. D. (2012). Interferon-inducible effector mechanisms in cell-autonomous immunity. *Nature Reviews Immunology*, 2, 367–382. <https://doi.org/10.1038/nri3210>
- Pawlowski, N., Khaminets, A., Hunn, J. P., Papic, N., Schmidt, A., Uthaiiah, R. C., Lange, R., Vopper, G., Martens, S., Wolf, E., & Howard, J. C. (2011). The activation mechanism of Irga6, an interferon-inducible GTPase contributing to mouse resistance against *Toxoplasma gondii*. *BMC Biology*, 9, 7. <https://doi.org/10.1186/1741-7007-9-7>
- Pettersen, E. F., Goddard, T. D., Huang, C. C., Couch, G. S., Greenblatt, D. M., Meng, E. C., & Ferrin, T. E. (2004). UCSF chimera: A visualization system for exploratory research and analysis. *Journal of Computational Chemistry*, 25, 1605–1612. <https://doi.org/10.1002/jcc.20084>
- Praefcke, G. J., & McMahon, H. T. (2004). The dynamin superfamily: Universal membrane tubulation and fission molecules? *Nature Reviews. Molecular Cell Biology*, 5, 133–147. <https://doi.org/10.1038/nrm1313>
- Prakash, B., Praefcke, G. J., Renault, L., Wittinghofer, A., & Herrmann, C. (2000). Structure of human guanylate-binding protein 1 representing a unique class of GTP-binding proteins. *Nature*, 403, 567–571. <https://doi.org/10.1038/35000617>
- Reese, M. L., Shah, N., & Boothroyd, J. C. (2014). The toxoplasma pseudokinase ROP5 is an allosteric inhibitor of the immunity-related GTPases. *The Journal of Biological Chemistry*, 289, 27849–27858. <https://doi.org/10.1074/jbc.M114.567057>
- Reese, M. L., Zeiner, G. M., Saeij, J. P. J., Boothroyd, J. C., & Boyle, J. P. (2011). Polymorphic family of injected pseudokinases is paramount in toxoplasma virulence. *Proceedings of the National Academy of Sciences of the United States of America*, 108, 9625–9630. <https://doi.org/10.1073/pnas.1015980108>
- Saeij, J. P., & Frickel, E. M. (2017). Exposing *Toxoplasma gondii* hiding inside the vacuole: A role for GBPs, autophagy and host cell death. *Current Opinion in Microbiology*, 40, 72–80. <https://doi.org/10.1016/j.mib.2017.10.021>
- Saijo-Hamano, Y., Sherif, A. A., Pradipta, A., Sasai, M., Sakai, N., Sakihama, Y., Yamamoto, M., Standley, D. M., & Nitta, R. (2021). Structural mechanism of PVM recognition by Irgb6. *Life Science Alliance*, 5, e202101149. <https://doi.org/10.26508/lsa.202101149>
- Sasai, M., Pradipta, A. M., & Yamamoto, M. (2018). Host immune responses to *Toxoplasma gondii*. *International Immunology*, 30, 113–119. <https://doi.org/10.1093/intimm/dxy004>
- Sastry, G. M., Adzhigirey, M., Day, T., Annabhimoju, R., & Sherman, W. (2013). Protein and ligand preparation: Parameters, protocols, and influence on virtual screening enrichments? *Journal of Computer-Aided Molecular Design*, 27, 221–234. <https://doi.org/10.1007/s10822-013-9644-8>
- Scharton-Kersten, T. M., Yap, G., Magram, J., & Sher, A. (1997). Inducible nitric oxide is essential for host control of persistent but not acute infection with the intracellular pathogen *Toxoplasma gondii*. *The Journal of Experimental Medicine*, 185, 1261–1274. <https://doi.org/10.1084/jem.185.7.1261>
- Shpetner, H. S., & Vallee, R. B. (1992). Dynamin is a GTPase stimulated to high levels of activity by microtubules. *Nature*, 355, 733–735. <https://doi.org/10.1038/355733a0>
- Steinfeldt, T., Konen-Waisman, S., Tong, L., Pawlowski, N., Lamkemeyer, T., Sibley, L. D., Hunn, J. P., & Howard, J. C. (2010). Phosphorylation of mouse immunity-related GTPase (IRG) resistance proteins is an evasion strategy for virulent *Toxoplasma gondii*. *PLoS Biology*, 8, e1000576. <https://doi.org/10.1371/journal.pbio.1000576>
- Uthaiiah, R. C., Praefcke, G. J., Howard, J. C., & Herrmann, C. (2003). IIGP1, an interferon-gamma-inducible 47-kDa GTPase

- of the mouse, showing cooperative enzymatic activity and GTP-dependent multimerization. *The Journal of Biological Chemistry*, 278, 29336–29343. <https://doi.org/10.1074/jbc.M211973200>
- Yamada, H., Abe, T., Nagaoka, H., Takashima, E., Nitta, R., Yamamoto, M., & Takei, K. (2022). Recruitment of Irgb6 to the membrane is a direct trigger for membrane deformation. *Frontiers in Cellular and Infection Microbiology*, 12, 992198. <https://doi.org/10.3389/fcimb.2022.992198>
- Yamamoto, M., Okuyama, M., Ma, J. S., Kimura, Y., Kamiyama, N., Saiga, H., Ohshima, J., Sasai, M., Kayama, H., Okamoto, T., Huang, D. C., Soldati-Favre, D., Horie, K., Takeda, J., & Takeda, K. (2012). A cluster of interferon- $\gamma$ -inducible p65 GTPases plays a critical role in host defense against *Toxoplasma gondii*. *Immunity*, 37, 302–313. <https://doi.org/10.1016/j.immuni.2012.06.009>
- Yamashita, K., Hirata, K., & Yamamoto, M. (2018). KAMO: Towards automated data processing for microcrystals. *Acta Crystallographica Section D: Structural Biology*, 75, 441–449. <https://doi.org/10.1107/S2059798318004576>

## SUPPORTING INFORMATION

Additional supporting information can be found online in the Supporting Information section at the end of this article.

**How to cite this article:** Okuma, H., Saijo-Hamano, Y., Yamada, H., Sherif, A. A., Hashizaki, E., Sakai, N., Kato, T., Imasaki, T., Kikkawa, S., Nitta, E., Sasai, M., Abe, T., Sugihara, F., Maniwa, Y., Kosako, H., Takei, K., Standley, D. M., Yamamoto, M., & Nitta, R. (2024). Structural basis of Irgb6 inactivation by *Toxoplasma gondii* through the phosphorylation of switch I. *Genes to Cells*, 29(1), 17–38. <https://doi.org/10.1111/gtc.13080>